DISSERTATIONS IN
FORESTRY AND
NATURAL SCIENCES

KIMMO KARHUNEN

# *Electrical Resistance Tomography Imaging of Concrete*

PUBLICATIONS OF THE UNIVERSITY OF EASTERN FINLAND
*Dissertations in Forestry and Natural Sciences*

UNIVERSITY OF
EASTERN FINLAND

**KIMMO KARHUNEN**

# *Electrical resistance tomography imaging of concrete*

Publications of the University of Eastern Finland
Dissertations in Forestry and Natural Sciences
No 122

Academic Dissertation
To be presented by permission of the Faculty on Natural Sciences and Forestry
for public examination in the Auditorium ML1 in Medistudia Building at the
University of Eastern Finland, Kuopio, on October, 3, 2013,
at 12 o'clock noon.

Department of Applied Physics

Kopijyvä
Kuopio, 2013
Editor: Prof. Pertti Pasanen, Prof. Kai-Erik Peiponen,
Prof. Matti Vornanen, Prof. Pekka Kilpeläinen

Distribution:
University of Eastern Finland Library / Sales of publications
P.O. Box 107, FI-80101 Joensuu, Finland
tel. +358-50-3058396
http://www.uef.fi/kirjasto

ISBN: 978-952-61-1232-9 (printed)
ISSNL: 1798-5668
ISSN: 1798-5668
ISBN: 978-952-61-1233-6 (pdf)
ISSN: 1798-5676

Author's address:
University of Eastern Finland
Department of Applied Physics
P.O.Box 1627
FI-70211 Kuopio
Finland
email: kimmo.karhunen@uef.fi

Supervisors:
Docent Aku Seppänen, PhD
University of Eastern Finland
Department of Applied Physics
70211 Kuopio
Finland
email: aku.seppanen@uef.fi

Professor Jari Kaipio, PhD
University of Eastern Finland
Department of Applied Physics
Finland
email: jari@math.auckland.ac.nz

Anssi Lehikoinen, PhD
Rocsole Ltd
Finland
email: anssi.lehikoinen@rocsole.com

Reviewers:
Associate Professor Daniel Watzenig, Dr.techn.
Graz University of Technology
Institute of Electrical Meas. and Meas. Signal Proc.
Inffeldgasse 22/II
A-8010 Graz
email: daniel.watzenig@tugraz.at

Christiane Maierhofer, Dr.
BAM - Federal Institute for Mat. Research and Testing
12200 Berlin
Germany
email: christiane.maierhofer@bam.de

Opponent:
Professor Matti Lassas, Ph.D.
University of Helsinki
Department of Mathematics and Statistics
P.O.Box 68
FI-00014 Helsinki
Finland

## ABSTRACT

Cracking and deterioration of concrete are the leading causes of a premature failing of reinforced concrete structures. To assess the condition of concrete, a variety of destructive and non-destructive testing methods have been developed. From these two methods, the non-destructive testing (NDT) is a more favorable (albeit more challenging) option since the tested target is left undamaged. The NDT modalities include acoustic, electromagnetic and radiation based techniques. In this thesis, the feasibility of electrical resistance tomography (ERT) for NDT of concrete is studied. In ERT, electric currents are injected into the target through electrodes that are are attached to the boundary of the target. The resulting voltages between the electrodes are measured and this boundary voltage data is then used to reconstruct the internal conductivity distribution of the target. The reconstruction of the internal conductivity distribution of concrete is expected to provide valuable information about the condition of the structure so that appropriate repairs can be taken in time.

The difficulty in ERT, as is in any other diffuse tomography modality, is that the problem has a nature of an ill-posed inverse problem. This implies that the solutions of the problem are unstable and nonunique in the classical sense. As a consequence, extra attention must be directed to the mathematical modeling of the measurements as well as to the reconstruction methods. Furthermore, concrete is strongly heterogeneous material composed of cement matrix, aggregate and different chemical compounds that create a challenging target for electrical modalities.

Previous studies have shown that ERT is a potential tool for NDT of concrete, but the quality of the reconstruction was not yet sufficient for practical applications. In this thesis, especially localizing reinforcing bars and crack identification are considered. To meet those aims, novel computational methods for the image reconstruction are developed. For the crack identification and localizing reinforcing bars, a novel adaptive meshing approach was developed. In the new approach cracks and reinforcing bars are modeled as internal structures. The results show that by employing accurate mathematical models and statistical inversion techniques based on the Bayesian framework, ERT can become an applicable tool for practical NDT of concrete.

*Universal Decimal Classification: 537.311.6, 620.179.1, 620.19, 621.3.011.2, 621.317.33, 691.32*

*INSPEC Thesaurus: nondestructive testing; flaw detection; concrete; imaging; tomography; electric impedance imaging; electric resistance measurement; electrical conductivity; inverse problems; image reconstruction; Bayes methods*

*Yleinen suomalainen asiasanasto: rikkomaton aineenkoetus; kuntokartoitus; betoni; betonirakenteet; kuvantaminen; tomografia; resistanssi; sähkönjohtavuus; impedanssitomografia; bayesilainen menetelmä*

# *Acknowledgements*

This work was carried out in the Department of Applied Physics at the University of Eastern Finland during the years 2007–2013.

I am very grateful to my main supervisor, Docent Aku Seppänen for his guidance and constant support during this work. I wish to express my gratitude to my second supervisor, Professor Jari Kaipio for his valuable advice and the opportunity to work in his excellent research group at the Department of Applied Physics. I also want to thank my third supervisor Anssi Lehikoinen, PhD, for his guidance and giving me the opportunity to work with ERT of concrete.

I want to give my best thanks to the official reviewers Associate Professor Daniel Watzenig, Dr., and Dr. Christiane Maierhofer for carefully reading the manuscript and providing excellent suggestions and comments.

I thank the staff of the Department of Applied Physics for their support. Especially, I wish to thank the members of the Inverse Problems group for fruitful collaboration and friendly working atmosphere. Many thanks to my colleagues and former roommates Antti Nissinen, PhD, and Antti Lipponen, MSc, for friendship and inspirational ideas. Equal thanks to my colleagues Ville Rimpiläinen, PhD, Teemu Luostari, MSc, and Gerardo Del Muro Gonzáles, MSc, for your support and friendship. Special thanks goes to Tuomo Savolainen, PhD, and Mr. Jukka Laakkonen for their invaluable help with measurement devices and technical issues.

I want to thank my co-author Associate Professor Nuutti Hyvönen for fruitful collaboration. I wish to thank my other co-authors, Professor Paulo Monteiro and Josh Blunt, PhD, for their collaboration and help to explore strange new world in the field of civil engineering and also for all the assistance during my visits to University of California Berkeley.

Naturally, I am grateful to my parents Erkki and Arja, my brother Ari and sister Heli and her family for all the support they have given. I also thank all my relatives and friends for their support and friendship.

Finally, I want to acknowledge the Finnish Funding Agency for Technology and Innovation (TEKES) and the collaborating companies in BETOMO project. I also acknowledge Emil Aaltosen säätiö for the financial support.

Kuopio, August 26, 2013 *Kimmo Karhunen*

## ABBREVIATIONS

| | |
|---|---|
| 1D | One-dimensional |
| 2D | Two-dimensional |
| 3D | Three-dimensional |
| AC | Alternating current |
| AE | Acoustic emission |
| CCP | Continuosly conducting path |
| CEM | Complete electrode model |
| C-H-S | Calcium silicate hydrate |
| CM | Conditional mean |
| CT | Computerized tomography |
| Cu-$CuSO_4$ | Copper-Copper sulphate |
| DC | Direct current |
| DCP | Discontinuously conducting path |
| EIS | Electrical impedance spectroscopy |
| EIT | Electrical impedance tomography |
| ERT | Electrical resistance tomography |
| FBP | Filtered backprojection |
| FE | Finite element |
| FEM | Finite element method |
| FRC | Fiber reinforced concrete |
| FRP | Fiber reinforced polymer |
| GN | Gauss-Newton |
| GPR | Ground penetrating radar |
| ICP | Insulating path |
| IE | Impact echo |
| IR | Infrared |
| ITZ | Interfacial transition zone |
| KIT4 | Kuopio impedance tomography 4 |
| LS | Least squares |
| MAP | Maximum a posterior |
| MCMC | Markov chain monte carlo |
| ML | Maximum likelihood |
| NDT | Non-destructive testing |
| PDE | Partial differential equation |
| Rebar | Reinforcing bar |
| RMS | Root mean square |
| w/c | Water to cement ratio |

## NOMENCLATURE

| | |
|---|---|
| $\|\cdot\|^2$ | $L_2$-norm |
| $(\cdot)_*$ | Expectation value |
| $(\cdot)_{\text{MAP}}$ | Maximum a posterior estimate |
| $\nabla(\cdot)$ | Gradient operator |
| $\nabla\cdot(\cdot)$ | Divergence operator |
| $A$ | Finite element system matrix |
| $\bar{b}$ | Downwards pointing normal |
| $\mathcal{C}$ | Basis matrix for electrode potentials |
| $D_l$ | Domain of $l^{\text{th}}$ internal inclusion |
| $d_{\text{c}}$ | Crack depth |
| $e$ | Gaussian distributed measurement noise |
| $e_\ell$ | Surface of the $\ell^{\text{th}}$ electrode |
| $F(\cdot\,;V)$ | Functional related to MAP-estimate |
| $f$ | Finite element data vector |
| $f_c$ | Characteristic frequency |
| $I_\ell$ | Electric current through the $\ell^{\text{th}}$ electrode |
| $\mathcal{I}$ | Total electric current vector |
| $J_{(\cdot)}$ | Jacobian matrix |
| $J_l$ | Electric current through $l^{\text{th}}$ internal inclusion |
| $L_{(\cdot)}$ | Cholesky factor |
| $l_{\text{c}}$ | Crack length |
| $\mathcal{M}$ | Measurement matrix |
| $N$ | Number of nodes |
| $N_D$ | Number of internal inclusions |
| $N_{el}$ | Number of electrodes |
| $\mathcal{N}(\cdot,\Gamma_{(\cdot)})$ | Normal (Gaussian) distribution |
| $n_j$ | Finite element basis function for electrode potentials |
| $\bar{n}$ | Outward unit normal |
| $\bar{n}_c$ | Crack normal |
| $R(\cdot)$ | ERT forward model |
| $R_0$ | Bulk resistance |
| $\mathcal{R}$ | Resistance matrix |
| $\mathbb{R}^d$ | $d$-dimensional real space |
| $U_h$ | Finite element approximation of electrode potentials |
| $U_\ell$ | Electric potential of the $\ell^{\text{th}}$ electrode |
| $\mathcal{U}$ | Total electric potential vector |
| $u$ | Electric potential |

| | |
|---|---|
| $u_h$ | Finite element approximation of electric potential |
| $u_i$ | Finite element coefficient of electric potential |
| $\tilde{u}_j$ | Finite element coefficient of electrode potentials |
| $\bar{u}$ | Finite element solution vector |
| $V$ | Voltage matrix for all current injections |
| $\mathcal{V}$ | Voltage matrix for one current injection |
| $W_l$ | Electric potential of $l^{\text{th}}$ internal inclusion |
| $x$ | Point in $\mathbb{R}^3$ |
| $x_1^{\text{c}}$, $x_2^{\text{c}}$, $x_3^{\text{c}}$ | Cartesian coordinates of crack position |
| $z_\ell$ | Contact impedance of the $\ell^{\text{th}}$ electrode |
| $\alpha$ | Angle of impedance plot arcs |
| $\beta$ | Crack angle |
| $\Gamma_{(\cdot)}$ | Covariance matrix |
| $\Delta\theta_k$ | Perturbation of $k^{\text{th}}$ crack parameter |
| $\delta_\xi^{(i)}$ | Search direction vector of $i^{\text{th}}$ iteration |
| $\zeta_l$ | Contact impedance of $l^{\text{th}}$ internal inclusion |
| $\theta$ | Crack parametrization vector |
| $\lambda^{(i)}$ | Step size of $i^{\text{th}}$ iteration |
| $\xi$ | Vector of unknowns |
| $\pi(\cdot)$ | Probability density |
| $\rho$ | Resistivity of a material |
| $\sigma$ | Conductivity of a material |
| $\sigma_h$ | Finite element approximation of conductivity |
| $\sigma_j$ | Finite element coefficient of conductivity |
| $\Phi$ | Stacked vector of unknowns |
| $\varphi_i$ | Finite element basis function for electric potential |
| $\phi_i$ | Finite element basis function for conductivity |
| $\Omega$ | Domain in $\mathbb{R}^3$ |
| $\partial\Omega$ | Boundary of domain |

## LIST OF PUBLICATIONS

This thesis consists of an overview and the following four original articles, which are referred to in the text by their Roman numerals **I–IV**.

**I** K. Karhunen, A. Seppänen, A. Lehikoinen, P.J.M. Monteiro and J.P. Kaipio, "Electrical resistance tomography imaging of concrete," *Cement and Concrete Research* **40,** 137–145 (2010).

**II** K. Karhunen, A. Seppänen, A. Lehikoinen, J. Blunt, J.P. Kaipio and P.J.M. Monteiro, "Electrical resistance tomography for assessment of cracks in concrete," *ACI Materials Journal* **107,** 523–531 (2010).

**III** N. Hyvönen, K. Karhunen and A. Seppänen, "Fréchet derivative with respect to the shape of an internal electrode in Electrical Impedance Tomography," *SIAM Journal on Appied Mathematics* **70,** 1878–1898 (2010).

**IV** K. Karhunen, A. Seppänen and J.P. Kaipio, "An adaptive meshing approach for localization of cracks with electrical impedance tomography," In Review *Inverse Problems and Imaging* (2013).

## AUTHOR'S CONTRIBUTION

All publications are result of collaboration with the co-authors. The author was the principal writer of the publications **I**, **II**, **IV** and a co-author in publication **III**. The author implemented all the numerical computations using MATLAB® and computed all the results in **I**, **II** and **IV**. In **III**, the author implemented the main part of the codes for the computational results of the paper. The author conducted all the measurements in these publications. The finite element package for solving the ERT forward problem is an adaption of the codes previously developed in the inverse problems group in the Department of Applied Physics.

# *Contents*

# 1 Introduction

Concrete is the most used building material in the world [1]. In 2008, the United States alone consumed 93.6 million tons of portland cement [2], and around 10 billion tons of concrete are estimated to be made in the world each year — that is over one cubic meter per every person on earth. The current concrete infrastructure throughout the western world dates to mid 50's. As the deterioration rates of this infrastructure are increasing, the pressure on civil engineering community in a form of structural evaluation, repairs and retrofitting is significant. It is estimated that 35 % of the work in building sector is directed to evaluation and repairs of damaged structures, and the percentage continues to increase [3]. Therefore, the development of new testing methods for faster and more reliable condition evaluation of concrete structures is critical. Techniques that provide information on the location of the reinforcing bars, the degree of cracking in the reinforced concrete, the distribution of chlorides in the matrix, the humidity gradients in concrete, the state of corrosion, and the depth of cover, are needed.

The testing methods for concrete can be divided in destructive and non-destructive methods. The destructive methods are usually mechanical and used for assessing the strength of concrete. Examples of destructive methods are core tests, pull-out test, pull-off tests and penetration resistance tests [4]. The Core tests are the most reliable, but cause the biggest damage for the inspected structure. In core tests, a sample (i.e. core) is extracted from concrete by drilling and then analyzed in laboratory. The pull-out and pull-off tests usually measure the force needed to remove different embedded or glued inserts from concrete. They can provide information about the compressive strength (pull-out test) or tensile strength (pull-off test) of concrete [4]. The penetration resistance tests (also known as the *Windsor probe* tests) use powder-actuated tools to fire nails or probes made of hardened steel alloys into the concrete. The strength of concrete is determined from the depth of penetration. Although destructive testing methods are reliable and easy to interpret, their biggest disadvantage is that the tested material has to be repaired. Substantial amount of time and money can be wasted in the repairs causing stress for the contractors to finish their project in time. Due to the high costs, the measurements are typically acquired from rather sparse coverage of the tested structures.

Non-destructive testing (NDT) methods are highly valuable for assess-

ing the condition of concrete without further impairing the tested structure. As a consequence, the expenses of the repairs in time and money can be avoided. The simplest, fastest and probably the most important non-destructive test is visual inspection. A well trained eye can provide valuable information from the types of cracking, spalling, colour changes etc. However, the visual inspection method is limited to detection of flaws on surfaces and, in the end, by the capabilities of human senses. Thus, more sophisticated methods for NDT of concrete have been developed. The NDT methods commonly in use are based on acoustical waves, electromagnetic techniques and different types of radiation, such as X-rays or infrared light. A review of the NDT methods is given in Chapter 3.

In this thesis, non-destructive testing of concrete with electrical methods is considered. Numerous studies during the last few decades have indicated that electrical methods are sensitive to various properties of concrete and are well suited for inspecting large concrete structures. Electrical (AC) impedance spectroscopy (EIS) is one of the most employed electrical methods. EIS has been applied for detection of cracks [5, 6], fiber distributions [7–9], fiber orientations [10], and corrosion rate of reinforcing bars [11–14]. Furthermore, AC impedance measurements can yield information about concrete humidity [15,16] and chloride distributions [17,18]. However, what EIS and most of the NDT methods are lacking, is realistic modeling of measurements. For instance, often the geometry and the inhomogeneities of the concrete properties within the target are not modeled accurately. This can lead to unreliable estimates for the concrete properties.

Electrical resistance tomography (ERT) [19–22] is a non-invasive imaging modality in which the aforementioned issues can be taken into account. In ERT, a set of electrodes is attached to the surface of the target. Electric current is applied through the electrodes, and the potential differences produced on the surface are measured using several electrode pairs. Based on these measurements, an estimate for the 3D distribution of resistivity (or its reciprocal, conductivity) is computed. Previously, ERT has been applied, for example, in process monitoring [23–26], biomedical imaging [27–31], geology [32–34] and some NDT applications [35]. However, only few preliminary studies for applying ERT to non-destructive testing of concrete or other cement based materials have been reported so far [36–39].

The reconstruction of the conductivity distribution in ERT is an *ill-posed inverse problem* [40, 41]. The practical definition of inverse ill-posed problems is that they are drastically sensitive even to moderately small

measurement and modeling errors. A powerful approach to ill-posed inverse problems is the Bayesian (statistical) framework [22, 40, 41]. In the Bayesian formalism, the uncertainties and errors in the measurements and models, as well as the properties of the primary unknown (conductivity) distribution, are modeled explicitly using statistical models. The explicit statistical models for the primary unknown are referred to as prior models or priors. The selection of the prior model depends on the prior information about the target and also on the tolerable complexity level of the associated numerical scheme needed to solve the inverse problem. The solution of the inverse problem can be obtained by combining the information given by the measurements with the prior model and the statistical measurement model.

In this thesis, the feasibility of ERT for 3D imaging of concrete is studied. Different geometries and internal structures are considered. The challenge of imaging a material with highly complex heterogeneous internal structure is addressed by developing and employing state-of-the-art computational models and inversion methods. The conducted numerical and experimental studies demonstrate that accurate modeling of the measurements and utilization of structural prior models with sophisticated numerical techniques can yield feasible reconstructions of the concrete conductivity as well as location and size of steel reinforcing bars (rebars) and cracks in concrete.

## Aims and contents of this thesis

The aims of this thesis are

1. To study the feasibility of ERT for imaging concrete. The feasibility of the method is verified with experimental data. In the experiment, concrete specimens with different embedded objects exhibiting resistive and conductive characteristics are considered.

2. To investigate the applicability of ERT for detection of cracks in concrete. Concrete beams and slabs, especially, are considered. In these geometries, the measurements are acquired from one surface only.

3. To take a novel computational approach to ERT to localize rebars and to estimate their sizes. For the estimation, an accurate rebar model and an adaptive meshing scheme are developed. The method is verified by numerical simulations.

4. To apply the adaptive meshing approach for crack identification. Especially, the estimation of crack depth and orientation in materials with inhomogeneous background conductivity is considered. The proposed approach is evaluated with numerical and experimental data.

This thesis is organized as follows. In Chapter 2, the basic characteristics of concrete in macroscopic and microscopic levels are discussed. In addition, the electrical properties as well as degradation of concrete infrastructure are considered. In Chapter 3, the NDT-methods currently in use for concrete are briefly reviewed. Chapter 4 describes the background of ERT. The discussion covers the electrode model, typical measurement techniques and outlines a reconstruction method that is based on Bayesian framework. In Chapter 5, ERT imaging of concrete is discussed. The feasibility of the method for imaging concrete as well as localizing rebars and cracks is evaluated by experimental and simulational studies. The conclusions are given in Chapter 6.

# 2 Concrete

The history of concrete construction is as old as 5600 years dating back to early concrete-like structures found from former Yugoslavia. The first major use of concrete was during the ancient Egyptian civilization, but what is modernly understood as concrete construction was achieved by the Roman empire over 2000 years ago. Perhaps the most famous example from Roman era is the Pantheon and its large concrete dome. As the Roman empire fell, the knowhow to build concrete structures was long forgotten until rediscovered in around the first half of the nineteenth century in England. Nowadays, concrete is the most extensively used construction material in the world. The applications of concrete concerns structures such as buildings, bridges, sewers and large pipes, dams etc.

In this chapter, the basic characteristics of concrete are reviewed to provide information about the macroscopic and microscopic composition of concrete as well as electrical properties that are largely determined by the pore structure in the microstructural level of concrete. In addition, reinforced concrete and the deterioration processes are also shortly considered. The discussion is mainly based on reference [1].

## 2.1 STRUCTURE OF CONCRETE

Concrete is a stone-like construction material mainly composed of cement, coarse and fine aggregate (i.e. gravel or crushed rocks and sand), water and some chemical admixtures. The fine and coarse aggregate form the bulk of the concrete and they are bonded together by hardened cement paste. The cement paste is a mix of cement and water which hardens through a chemical reaction known as *hydration*. This is the key feature of concrete; the newly mixed concrete is plastic and malleable, which enables it to flow easily into preforms of various shapes, yet strong and durable when hardened. In Figure 2.1, a cross section from concrete specimen shows the two macroscopic phases that are the aggregate and the cement paste. The Figure 2.1 shows also air voids that have been entrapped in the concrete batch during casting.

The careful proportioning and mixing of the ingredients is essential in achieving strong and durable concrete. The proportions should be designed such that the concrete mixture retains the desired workability of freshly mixed concrete and the required strength for the hardened con-

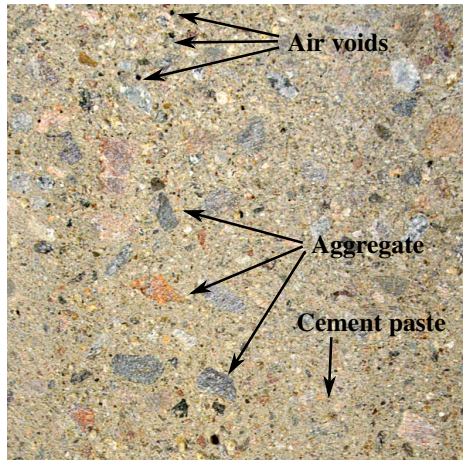


*Figure 2.1: Cross section from concrete specimen showing aggregates, cement paste and air voids.*

crete. Typically, a mix is about $60-75$ % of aggregate, $10-15$ % of cement and $15-20$ % of water by volume.

The typical measure of concrete strength is the compressive strength (measured in MPa) that defines the concretes ability to resist compressive stress. The main factor determining the strength of concrete is water-cement ratio $w/c$, although other factors such as curing conditions, aggregate sizes, admixture types, specimen geometry and moisture conditions along with stress types and loading can also have an effect on the strength. The types of concrete used in infrastructure are often divided into three classes [1]: low strength concrete (less than 20 MPa), moderate strength concrete (20-40 MPa) and high strength concrete (over 40 MPa). The most used concrete class in normal structural work is the moderate strength concrete, whereas the high-strength concrete has its applications in more special constructions.

It is a well known fact that concrete is strong in compression but considerably weaker in tension (the tensile strength of plain concrete is typically only about 10% of its compressive strength) and thus structures made of plain concrete are vulnerable to shear stresses caused by wind, earthquakes and other tensile forces. Therefore, virtually every modern concrete building is reinforced to bear the tensile load. The reinforcement types for concrete are reviewed in Section 2.3.

### 2.1.1 Composition

The aggregate material occupies the largest portion of the concrete mix volume and hence aggregates should be chosen carefully. The type and size distribution of aggregate mixture depends on the required characteristics and purpose of the final concrete product. In principle, the aggregate can be any granular material that takes no action in the hydration process and possess the required qualities in strength, density and durability. Commonly, materials such as sand, gravel, crushed stone, crushed blast-furnace slag, or construction and demolition waste are used for aggregate. The term coarse aggregate refers to aggregate particles of size larger than 4.75 mm, whereas the fine aggregate contains particles smaller than 4.75 mm but larger than 75$\mu$m [1].

Cement is a dry powder substance that is used to bind the aggregate materials of concrete. Cement alone is not a binder but upon the addition of water the binding property is developed as a result of hydration. Cements that harden by reacting with water and form a stable product that can resist wet weather or aqueous environments are called *hydraulic cements*. The most commonly used hydraulic cement is *portland cement*. The non-hydraulic cements (e.g. lime and gypsum plaster) are not stable in water and must be kept dry in order to gain strength.

The mixing water has an important role in concrete mixing as it initiates the hydration and controls the workability of concrete batch as well as the strength of the end result. The amount of water is indicated by a water-cement ratio $w/c$ that is given as a mass ratio. A low $w/c$ ratio yields concrete that is strong and durable whereas high ratio results freer flowing, malleable concrete with less strength. Typical $w/c$ ratios are 0.7 for low strength concrete, 0.5 for moderate strength concrete and 0.35 for high strength concrete [1]. The $w/c$ ratio largely determines the porosity of the hydrated cement paste, which is the key factor that contributes to the strength of concrete. Depending on the porosity of the cement paste and the environmental humidity, large amount of water in different forms can exist in concrete. Although the amount of water decreases with drying and progressing hydration, not all water is lost during aging or even on extreme drying. A more detailed review of water in the microstructural level of concrete is given in Section 2.1.2.

The chemical admixtures are added to the concrete batch at the time of mixing to control various characteristics of concrete that are not achievable with plain cement-water mixes. For example, the admixtures are often used to improve the workability of fresh concrete or increase the density

and strengthness, and enhance the durability of hardened concrete. In cold environments, air entrainment admixtures are valued by their ability to increase the porosity of concrete which results in concrete that is highly resistant to freezing and thawing cycles.

Concrete gains most of its strength during the first few days and weeks after it has been placed. During this period, it is critical to maintain proper conditions for concrete to harden fully. This maintenance is known as *curing*. The main aim in curing is to keep the temperature and moistness high enough that the hydration happens effectively. Improper curing would essentially lead to reduced strength of concrete. Excessive premature drying, especially, can yield *shrinkage cracking* when water evaporates from the pores thus causing internal stresses that concrete cannot withstand in its early stage of hardening.

### 2.1.2 Microstructure of concrete

Concrete has a highly heterogeneous and complex microstructure that comprises three major components, namely, hydrated cement paste, aggregate and the transition zone between cement paste and aggregate [1]. Regarding an electrical NDT of concrete, the cement paste and the transition zone, and the pore water within, are the most important. Hence, only these two components are covered in the following discussion. The forms in which water exists in the pore structure at the microstructural level of the cement paste are also considered. The electrical properties of concrete are discussed in Section 2.2.

The hydration process in concrete is the reaction between water and cement. The hydration reaction starts immediately upon the addition of water. During this reaction, microscopic needle-like crystals, or nodes, form on the surface of cement particles. As the nodes grow, they attach to nearby aggregates, steel reinforcement or to nodes from other particles. With the addition of water to concrete mix, the average distance between particles increases and less linking between the nodes can happen. Thus, the more water is used in the mixing, the less stronger, yet more workable, hardened concrete will be, and vice versa. Most of the hardening takes place within the first month of concrete's lifetime, but in theory the hydration process continues for years (or even the entire lifetime of concrete).

The hydrated cement paste is a complicated compound containing several solid phases. The most significant phases are the calcium silicate hydrate gel (C-S-H phase) which provides the strength and calcium hydroxide crystals which contribute to alkalinity of cement [1]. The C-S-H

phase (also known as C-S-H gel or cement gel) contains very small interparticle space (gel pores) that are approximately from less than 1 nm to 10 nm in size. The other voids that exist in hydrated cement paste are capillary voids and air voids. The size of capillary voids can range approximately from 5 nm to 5 $\mu$m depending on the $w/c$ ratio and the degree of hydration. Capillary voids are formed by the external water that is not hydrated or absorbed by the gel pores. The formation of capillary voids depends heavily on the water-cement ratio. With a water-cement ratio less than 0.4 (approximately) the hydration process consumes most of the excess water thus reducing the number of capillary voids close to zero. The air voids generally differ from the irregular shaped capillary voids and share a spherical shape [42]. They are formed by either small bubbles entrained on purpose or air that is entrapped in concrete mix during casting. The size of entrained air voids range from 10 to 300 $\mu$m whereas the larger entrapped air voids can have a maximum size of 3 mm. The entrapped air voids usually exist near the surface because they are born between concrete mix and formwork.

The pore structure in cement paste is one of most important characteristics of concrete and strongly influences the strength and transport mechanism of concrete. While the entrained air voids are often desired because of their ability to compress and thus reduce external stress (for example, due to freezing), the capillary voids can be harmful and usually are undesired. With the help of capillar suction, the capillaries form a quick transit system for water and deleterious agents such as chloride and sulfate ions into the concrete [43]. The deterioration processes in concrete are briefly reviewed in Section 2.4.

The volume that exists between the large aggregates and the hydrated cement paste is called *interfacial transition zone* (ITZ). The composition of the ITZ is very similar to bulk cement paste, but it differs in microstructure and properties. In normal concrete, the porosity of the interfacial transition zone is much higher than that of the bulk cement paste [44]. This owes to the fact that water films tend to form around large aggregates (known as *internal bleeding*) increasing locally the water-cement ratio leading to higher porosity. Because the ITZ is what serves as the bridge between a coarse aggregate and the cement paste matrix, it is generally considered as the weakest link of the concrete matrix. Thus, it is the transition zone phase that ultimately determines the strength of concrete.

Water can exist in the hydrated cement paste in many forms. The categorization of different types is based on the degree of difficulty of removing water from concrete. In empty or partially filled voids, water

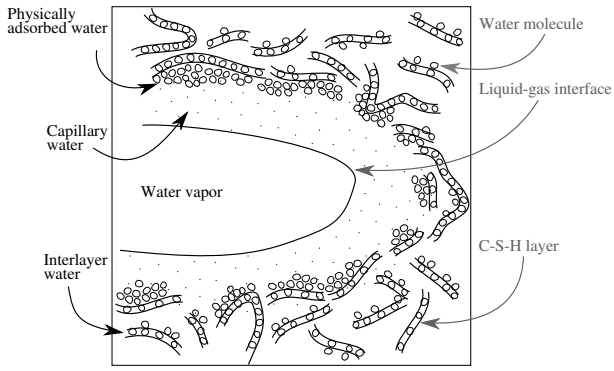


*Figure 2.2: Schematic representation of partially water-filled void and the types of water that exist in hydrated cement paste.*

exists as *water vapor* in equilibrium with the environmental humidity. In addition to vapor in voids, water is held in the hydrated cement paste in the following forms [1]: *Capillary water* is present in voids larger than about 5 nm. In large capillaries ($>$ 50 nm), water exists as a *free water* because its removal does not cause any volume change. In small capillaries (5 to 50 nm) the water is held by capillar tension and its removal may cause shrinkage of the system. *Adsorbed water* is physically adsorbed (as water molecules) to the solid surfaces in the C-S-H phase. Adsorbed water can be removed when drying in around 30 % relative humidity resulting in shrinkage of the hydrated cement paste. *Interlayer water* is associated with C-S-H structure as monomolecular layers between the layers of C-S-H. Interlayer water is lost only on strong drying around 11 % RH resulting considerably shrinkage of the C-S-H structure. *Chemically combined water* is an integral part of various hydration products and it can be removed only on decomposition during heating. The water types based on the model proposed by Feldman and Sereda [45], associated with the calcium silicate hydrate phase, are illustrated in Figure 2.2.

## 2.2 ELECTRICAL PROPERTIES OF CONCRETE

As explained in the previous section, concrete has a complex heterogeneous structure mainly composed of aggregate and cement paste. The cement paste itself is also a complex composition of a network of capillar cavities and C-S-H. The conduction of electric current through this system can take several paths with different characteristics. Over a wide

*Table 2.1: Typical resistivities $\rho$ and conductivities $\sigma$ for concrete in different environments at 20°C and for aggregate commonly used in concrete.*

| Material/environment | | $\rho$ (Ωm) | $\sigma$ (mS/cm) |
|---|---|---|---|
| Concrete[1,2] | Wet | 15 – 200 | 0.05 – 0.67 |
| | Outdoors (exposed) | 100 – 400 | 0.025 – 0.1 |
| | Outdoors (sheltered) | 200 – 500 | 0.02 – 0.05 |
| | Indoors (50% RH) | $> 3000$ | $< 3 \cdot 10^{-3}$ |
| Aggregate[3] | Quartz | $4 \cdot 10^4$ – $1 \cdot 10^{12}$ | $1 \cdot 10^{-11}$ – $2.5 \cdot 10^{-4}$ |
| | Granite | 5000 – $1 \cdot 10^6$ | $1 \cdot 10^{-5}$ – $2 \cdot 10^{-3}$ |
| | Sandstone | 180 – 4000 | $2.5 \cdot 10^{-3}$ – 0.056 |
| | Limestone | 300 – 1500 | 0.007 – 0.033 |

[1]According to Polder [47]
[2]According to McCarter et al. [46].
[3]According to Whittington et al. [48].
Note: $\sigma = \rho^{-1}$; 1 S/m = 10 mS/cm.

frequency range the complete electrical response of concrete is complex valued and denoted by the impedance of concrete. Although impedance modeling is needed to gain full understanding of the electrical response of concrete, it is common to use approximative real valued resistivity models, especially, in the 0.01 – 1000 Hz frequency range, where plain concrete acts as a pure resistor [12]. The resistivity of concrete is an important parameter that can provide information about the strength, degree of hydration and moisture content [46,47]. In addition, electrical measurements can provide information about local parameters of concrete such as cracks and location and corrosion of rebars. In the following, the electrical properties of concrete are briefly discussed.

Typical resistivities and conductivities of different concrete and aggregate types are listed in Table 2.1. It can be seen that the resistivities of the aggregates are several orders of magnitude higher than the resistivity of concrete. Thus, the aggregates are considered inert, non-conducting particles in a conducting cement paste matrix, and the conduction of current is largely determined by the hydrated cement paste and the randomly distributed, water-filled capillary pores within. The variation of the concrete resistivity in each environment in Table 2.1 is caused by the variation of $w/c$ ratio and chemical composition of the hydrated cement paste [47]. The increase in $w/c$ ratio shows up as decrease in resistivity. The resistivity also decreases with increasing temperature [46–48]. Further, the progressing hydration 1) chemically bonds more water 2) fills the capillar

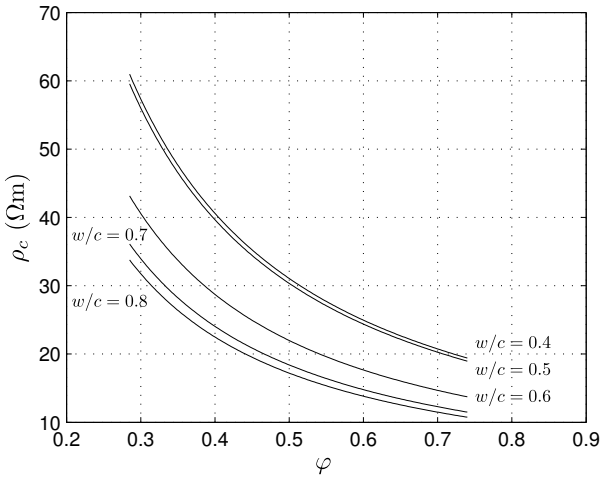


*Figure 2.3: Resistivity $\rho_c$ of young and moist concrete for different $w/c$-ratios as a function of fractional volume $\varphi$ of the cement paste. The plots are based on an experimentally determined equation $\rho_c(\varphi) = 1.04\rho_p\varphi^{-1.2}$, where $\rho_p$ is the resistivity of the paste with the same $w/c$-ratio and at the same age as the concrete. The equation and the $\rho_p$ data are from [48].*

pore space, thus blocking paths for electrical conduction. Hence, the resistivity of concrete increases during the hydration process. As a result, the resistivity (or conductivity) of concrete can be an indirect measure of its strength in at particular point in time.

The resistivity of different concrete mixes have been studied, for example, in [46, 48]. In these studies, it was found that the resistivity of concrete depends on the resistivity and on the fractional volume $\varphi$ of the cement paste. The higher the fractional volume of the paste, the less resistive the resulting concrete is. The resistivity of the cement paste is largely dictated by the $w/c$-ratio. Approximative graphs for concrete resistivity as a function of the fractional volume of the cement paste for different $w/c$-ratios are given in Figure 2.3. However, it should be noted that environmental variables have a significant effect on the concrete resistivity and the graphs presented in Figure 2.3 are approximative and applicable only to concrete mixes cured in controlled and moist conditions.

It is speculated [15, 48] that the mechanism of conduction through moist concrete is largely by means of ionic conduction in the evaporable water in the cement paste and to a lesser extent by means of electronic conduction through the cement compounds, such as the gel, gel-water

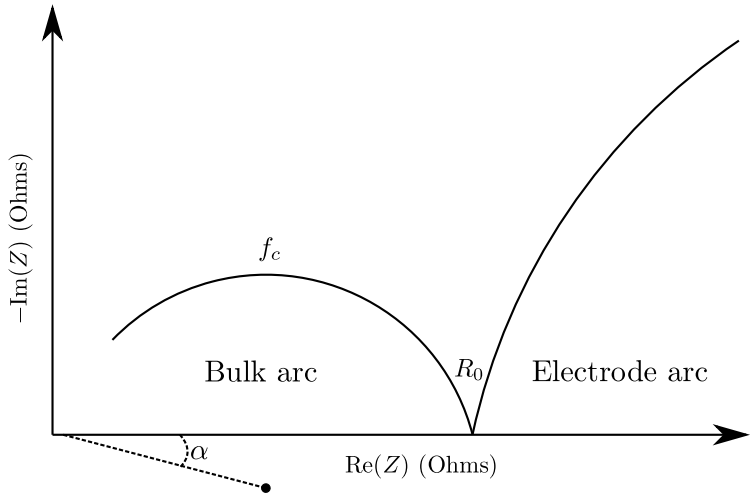


*Figure 2.4: Schematic representation of complex response for cementitious material. The frequency increases from right to left in counterclockwise fashion.*

and unreacted metallic compounds. However, it is noted that separation of these two mechanisms is virtually impossible since the electric conduction depends on the composition and concentration of ions in the evaporable water and the composition and structure of the solid phase, which are heavily linked to each other. In 1981, Whittington et al. [48] modeled the conduction paths through concrete with conductive paths that can have three possible paths, that is, through cement paste, through paste and aggregate in series and through aggregate particles in contact. However, it is extremely unlikely that aggregate particles would be in contact one by one with each other through the whole path. More recently, it has been postulated that the conduction of current through concrete can mainly take three paths forming continuously conducting paths (CCP), discontinuously conducting paths (DCP) and insulating paths (ICP) [49]. The CCPs are the paths with least resistance combining a series of capillary cavities that are connected by pore necks. Discontinuous paths (DCP) are a series of micro-pores whose continuity is blocked by cement paste layers. The insulating paths (ICP) are the paths through solid cement paste/aggregate structure.

The frequency dependent impedance response of cementitious materials (i.e. cement-pastes, limes, mortars, etc.) and concrete have been studied, for example, in [15,17,49–53]. It has been discovered that concrete

also exhibits a capacitive nature and the corresponding impedance plots are typically characterized by two semicircular arcs known as *bulk arc* and *electrode arc*, see Figure 2.4. The development of the bulk arc (typically over 1 kHz [52]) is a result of the capacitive behaviour due to the polarization effects in the pore structure of hardened concrete. It is the accumulation of the ions at the constrictions in the discontinuous paths (DCP) and pore necks that contribute to capacitive response. The development of the electrode arc at lower frequencies (typically below 1 kHz [52]) is a result of polarization effects in the measurement electrode and concrete interface. The centers of the arcs are depressed below the real axis by an angle $\alpha$ (here shown only for the bulk arc) because of the multiple relaxation frequencies over a wide frequency range in the polarization processes [54]. The bulk resistance (denoted by $R_0$) is determined by the point where the real axis and the low frequency arc intersect. The maximum value of the bulk arc on the imaginary axis occurs at the characteristic frequency $f_c$ (typically in the MHz range [52, 55]). It is speculated, that the value of $f_c$ and $\alpha$ could be related to the size and distribution of pores [54].

The addition of reinforcing material, such as steel rebars or fibers, into concrete has a significant effect on the electrical properties. Thus, it is often advised to localize the rebars first and then conduct the resistivity measurements of concrete as far as possible from the rebars [47]. The presence of steel rebars in concrete is observed as a local decrease in the resistivity and, especially, as transitions in the phase response [11]. With the addition of conductive fibers, the impedance plot shows two bulk arcs instead of one for plain concrete. This well known behaviour is called *dual-arc behaviour* and it occurs due to polarization effect on the conductive fibers [8].

Another factor that has an effect on electrical properties of concrete is the cracks. Almost all concrete have some form of cracking (see Section 2.4), which can be observed as a change in contrast of resistivity between the crack and surrounding concrete. The cracks can be either conductive (saturated with water) or insulating with respect to the concrete resistivity. The first case would correspond to moist cracks and the latter one for dry cracks. In the impedance plot (Figure 2.4) the cracks would locally change the $R_0$ point on the real axis.

## 2.3 REINFORCEMENT FOR CONCRETE

Although plain concrete itself is sometimes used in foundations, pavements, basement walls and even large scale structures such as dams and canal linings, the introduction of reinforced concrete have made possible most of modern concrete structures. The most common reinforcement material is steel, but other materials such as *fiber-reinforced polymer* (FRP) are also used [56]. An example of a reinforced concrete during construction is shown in Figure 2.5.

For increasing the tensile strength of concrete, two construction principles are used: *reinforced concrete* and *prestressed concrete*. The design of reinforced concrete is normally such that the concrete carries the compressive forces while the added reinforcing material handles the tensile forces. In prestressed concrete, the tensile stresses are reduced by introducing internal stresses through tendons that are tensioned and anchored to the concrete.

Steel is well suited for reinforcing concrete due to its high tensile strength and good bonding capability to concrete. The steel reinforcement is typically available as individual steel bars or as a rectangular mesh of wires factory welded at their intersections. In *Fiber-reinforced concrete* (FRC), small (10 – 75 mm in length) discrete fibers made of materials such as steel, glass, nylon, polyester, propylene and natural fibers are mixed with concrete. Fibers are added to concrete, especially, to reduce cracking due to plastic and drying shrinkage, that normal steel reinforcement cannot prevent. However, fibers do not generally increase the tensile strength of concrete. Fibers can also be used together with steel reinforcing bars. [56]

Prestressing can be achieved either by pre-tensioning or post-tensioning. In pre-tensioned concrete the steel tendons are tensioned before the concrete is placed and embedded into the concrete in their tensioned state. When the concrete is settled, cured and reached the required strength, the tensioned stresses are released. The disadvantage of pre-tensioning is that the most of the concrete elements have to be prefabricated at the factory, because strong anchoring points are needed during casting. Post-tensioned concrete differs from the pre-tensioned concrete in that the tendons are tensioned after the concrete has been placed. The prestressing force is transferred to the concrete by using end anchorages. The main benefit of post-tensioning over the pre-tensioning is that it can be performed at the jobsite. [56]

*Figure 2.5: Placement and compaction of concrete around embedded steel reinforcement on a rooftop in Helsinki, Finland.*

## 2.4 DETERIORATION OF CONCRETE STRUCTURES

Deterioration and failure of reinforced concrete structures is a frequent concern nowadays. The physical and chemical mechanisms of deterioration can be divided in numerous sub-categories acting in macro- and micro-levels. Often, these mechanisms are also superimposed on each other and thus hard to separate. The mechanisms contributing to deterioration of the reinforced concrete can be categorized, for example, as follows [57,58]:

- Incorrect selection of construction materials.
- Errors in design.
- Incorrect construction practices, inadequate quality control and supervision.
- Chemical attacks such as corrosion, carbonation, alkali-silica reaction and chloride, sulphate, salt and acid attacks.
- External physical and mechanical factors such as restraint against moving, cracking, abrasion, fire resistance and freezing and thawing.

In the following, the most important mechanisms regarding the applications aimed at in this thesis are considered. For more information about the subject, see the cited references above.

The most important single parameter that contributes to the degradation of concrete is water [1]. Water is able to penetrate deeply into the

porous structure of concrete and thus capable of transporting dissolved substances that are harmful to concrete. As a result, the strength and durability of concrete decreases which is often observed as cracking and reinforcement corrosion and, eventually, as a failure of the structure.

Cracking is one of the most fundamental reasons leading to premature failing of concrete structures. Cracking occurs due to mechanical loading or environmental effects, and virtually all concrete cracks. Cracks can be macrocracks which are observable by visual inspection, or microcracks that form at coarse-aggregate boundaries and propagate through the surrounding mortar in the microstructural level and consequently can be detected only with microscopic techniques or by non-destructive testing [59]. A significant parameter is the crack width. Large cracks (crack width $> 0.3$ mm) that remain open under tensile load can accelerate the corrosion of rebars because the harmful agents can easily penetrate the protective concrete cover through the crack [60]. On the other hand, it has been reported that crack widths under 0.3 mm have little impact on the rebar corrosion, thus not all cracking is severely detrimental [60]. Uncontrolled cracking, however, is always of a serious concern. It is essential, that the degree and nature of cracking are evaluated and proper repairs are undertaken before serious damage can happen. In this thesis, the detection of cracks using ERT is discussed in section 5.3.

Corrosion problems arise, for example, if structures are exposed to high concentrations of chlorides or reinforcements are misplaced due either to inadequate design or to incorrect construction practices. Misplacement of reinforcing steel may reduce the protective concrete cover, which results in an early initiation of the corrosion processes. The rebar corrosion can lead to serious cracking due to expanding corrosion products that increase internal stresses in concrete. Severe cracking reduces the structural capacity and in turn exposes the rebars for more rapid corrosion. Eventually, the badly corroded rebars cannot provide the additional strength needed to handle the tensile stresses and the reinforced concrete structure fails. Thus, the condition evaluation and localization of rebars is important. The localization of rebars using ERT is discussed in section 5.4.

# 3 Non-destructive testing of concrete

As discussed in previous chapter, concrete structures deteriorate in many ways. Hence, the condition assessment includes several testing problems such as crack identification, rebar corrosion and misplacement detection, determination of compressive strength, thickness measurements, assessment of delaminations and localization of grouting faults.

The testing of concrete structures can be conducted with numerous methods ranging from visual inspections and tapping/listening tests to highly developed three dimensional tomographic modalities. The testing methods can be destructive or non-destructive in nature, but the latter are preferred because of their cost-effectiveness, easiness of use and ability to leave the target undamaged.

The pool of non-destructive methods for concrete is rich, although the most advanced NDT-methods are still in development. Currently, there is no one all-purpose NDT-tool for concrete, but the modality has to be selected according to the application.

The aim of this chapter is to give a short introduction to the most prominent non-destructive modalities for concrete. The chapter is divided in three sections according the underlying physics of the methods: acoustic methods, methods that are based on radiation and electromagnetic methods. The discussion is mainly based on reviews [61–64]. For further reading, see e.g. [65–67].

## 3.1 ACOUSTIC TECHNIQUES

In this section, methods based on elastic wave propagation in solids, caused by acoustical or mechanical excitation are considered. The simplest form of testing in this category is the so-called "coin tap" test in which the wall is tapped with a lightweight hammer and the produced echo is observed by human ear for signs of imperfections inside the structure. A more sophisticated version of the tapping technique is a Schmidt hammer or a rebound hammer test, in which a spring loaded mass is impacted against concrete surface at defined energy and the rebound of the spring-mass system is measured [4]. Schmidt hammers provide qualitative measures of the surface condition of concrete. By calibrating the rebound measurements with core tests, the Schmidt hammers can be used to determine the approximate compressive strength of concrete.

Although the tapping and rebound tests are as simple techniques widely in use and are effective in detecting delaminations, debonds and uniformity of concrete, the methods are highly operator dependent and typically provide information only qualitative in nature. For quantitative and more accurate inspection, more sophisticated methods have been developed. The acoustical techniques can be divided in various subcategories. Below, the following methods are briefly reviewed: ultrasonic/ultrasonic pulse-echo, impact-echo and acoustic emission.

In ultrasonic techniques [68–71], the propagation and dispersion of high frequency (over 20 kHz) sonic waves are exploited in the investigation of the target. The ultrasonic waves are produced using ultrasonic transducers. Ultrasonic measurement systems can be divided in two main groups [72]: Transmission and pulse-echo systems. In transmission systems the source and receiving transducers are placed on the opposite surfaces of the tested target, whereas pulse-echo systems can be used for test subjects allowing only one-sided access to the target. Typical applications are localization of rebars and tendon ducts, fault detection and thickness measurements. Currently, ultrasonic techniques are among those few methods capable for producing 3D images of concrete and more or less the only technique that is applicable for on-site characterization of cracks [73–77]. A commercial version for 3D imaging is available as "Mira- ultrasonic concrete tomographer" [78]. Ultrasonic techniques usually have an excellent resolution. However, the dispersion of the waves from the heterogeneous structures of concrete limit the effective imaging depth of the ultrasonic methods.

Impact-echo (IE) method [61, 62, 79, 80] works similarly to pulse-echo methods, but instead of using ultrasonic transducers for excitation, a mechanical impact is produced by tapping a small steel sphere against the concrete surface. The mechanical impact induces elastic waves which are reflected from internal flaws and/or external surfaces. The reflected waves are then observed by accelerometers, displacement sensors or other sensors capable of measuring vibrations. In contrast to ultrasonic techniques, the mechanical impact creates waves with higher amplitudes thus allowing deeper penetration into concrete. However, the frequency range in impact-echo is low which results weaker resolution. Impact-echo method is useful for quick survey of the inspected area and the typical applications include thickness measurements, detection of flaws such as voids and delaminations in plate-like structures (bridge decks, slabs, walls, etc.) or concrete beams and columns. IE-method is well suited for inspecting reinforced concrete structures because of the long wavelength content of

the stress waves (typically between 50 mm – 2000 mm) that are weakly attenuated by the heterogeneous structure.

Acoustic emission (AE) [81, 82] is a monitoring technique that, as opposed to other acoustic methods, does not use controlled excitation to produce elastic waves into the material but instead passively monitors the local and rapid changes in elastic strain energy that show up as stress waves (i.e. acoustic emissions) in the material. The acoustic emissions can be generated by deformations and fractures and thus AE technique is suitable for continuous condition assessment of a structures. For example, AE has been used estimating the damage in reinforced concrete structures [83].

## 3.2 METHODS BASED ON RADIATION

Radiation can be either ionizing (e.g. X-rays) or non-ionizing (e.g. infrared waves). In NDT-methods that exploit ionizing radiation, the attenuated radiation is detected as the rays pass through the object. From this attenuation data, an image of the internal structure of an object is formed either directly as in radiography or through cross-sectional images as in computerized tomography (CT). Methods exploiting non-ionizing radiation, such as infrared thermography, use the part of the electromagnetic spectrum corresponding energies that are not high enough to ionize an atom. Normally these methods detect the radiation emanating from visible surfaces directly.

Typical NDT-modalities based on the ionizing radiation are radiography (X-ray, gamma-ray) [84], neutron radiography or tomography [85–87] and computerized tomography (CT) [88, 89]. In addition, backscattering techniques have been used [90]. Radiography is typically used for detecting porosity, air voids and other inclusions that differ in density and thickness influencing in the absorption of radiation. Neutron radiography has been studied for detection of cracks and microcracking in concrete. Computerized tomography uses either X-rays or $\gamma$-rays to form three dimensional images of the target and has its main applications in crack detection and inspection of embedded rebars. The spatial resolution is commonly superior to other tomographic modalities. However, the use of ionizing radiation always involves health hazard to personnel. This is especially a concern with concrete as high doses of radiation are needed to penetrate the target effectively. As a consequence, the use of X-rays is often impractical at the job site. For example, X-ray imaging of

a concrete bridge may require a zone radius to 1000 m cleared of humans and cattle, when high dosage X-ray instruments are used [61]. The safety precautions and the money spent in instruments capable of producing high energy radiation makes methods using ionizing radiation expensive. Neutron radiography and CT-imaging are mostly limited to small scale measurements in laboratory [61,62,87].

Infrared (IR) thermography [61,62,91,92] methods are used to detect the energy that is emitted as radiation in infrared region of the electromagnetic spectrum. The applications include detection of defects and finding heat losses. The principle in IR thermography imaging of flaws in concrete is that the defects such as delaminations and cracks increase the absorption of thermal energy on the surface which can be observed in the emitted IR-image as hot spots. The heat loss inspections of buildings can be conducted either as interior or exterior surveys. Usually, the interior scans are preferred because the warm air mass does not always escape through the walls in a straight line but moves in the open cavities of the wall structure before getting out. In such cases, exterior surveys can give misleading results. Also, the interior scans are not affected by weather variations. Infrared thermography is a fast, non-contacting modality and it does not require any health safety precautions. However, factors such as solar radiation, surface emissivity and weather variations complicate the quantitative assessment. Moreover, IR thermography surveys cannot provide information about the depth of the defects.

## 3.3 ELECTRICAL AND ELECTROMAGNETIC METHODS

This section covers the most common NDT methods that use electrical or electromagnetic excitation to gather data from the inspected structure. This discussion concerns the radar methods, electromagnetic covermeters, conductivity and resistivity measurements and half-cell potential measurements.

The most common use of electromagnetic methods is in determining the thickness of concrete cover over the rebars and the localization of rebars [93]. These methods are based on the fact that (embedded) metals placed in external electromagnetic field induce a change in that EM-field, which can be measured. The change in EM-field depends on the size, composition of metal and the thickness (cover) of the medium between the metal and the instrument. The commercial instruments based on these applications are known as covermeters [61]. Covermeters are sensitive to

conductivity variations in concrete and may loose accuracy when anomalous conductivities exist near the rebars (e.g. due to saline water penetration). Usually, covermeters do not need direct contact to the surface of the medium.

Ground penetrating radar (GPR, also known as sub-surface radar) [94, 95] is a powerful method that has been previously used extensively in geophysical applications. GPR exploits electromagnetic waves that are emitted through an antenna into the investigated structure and the reflected energy is recorded and analyzed. The data collection is non-contacting and can be performed by sliding the antenna over the target surface. As a consequence, GPR is a relatively fast modality and large areas can be measured in reasonable time. Typical applications of GPR are determining the element thickness or defects such as cracks and delaminations, moisture detection, detection of concrete cover and localization of reinforcement and tendon ducts [63, 94]. A drawback of GPR method is that due to the nature of electromagnetic waves the radar cannot penetrate metals. In addition, the data produced by GPR can be difficult to interpret and usually an experienced user is needed for analysis.

The resistivity (or conductivity) measurements of concrete have been conducted using both electrical direct current (DC) and alternating current (AC) measurements. Because of the electrode polarization, the DC measurements are usually carried out using a *Wenner-array* electrode configuration. The Wenner electrode array consist of four equally spaced electrodes in a line where the outer electrodes are used to inject current and the resulting voltages are measured between the inner electrodes. In the AC measurements, by contrast, only two electrodes are required. The basic idea of the electrical resistivity measurements is to map the local resistivity of concrete from the surface measurements. For inspecting large areas, the surface has to be scanned with the electrode array. Applications of the resistivity measurements are, for example, evaluation of rebar corrosion [96, 97], moisture content and salt content [17, 98]. Further, Lataste et al. have applied electrical resistivity measurements for localization of cracks [5] and characterizing steel fiber distributions [99]. McCarter et al. applied electrical AC measurements for monitoring water penetration, ionic ingress and moisture movement in cover zone concrete [100].

Perhaps the most widely studied electrical method is the electrical impedance spectroscopy (EIS). The basic operation of EIS is similar to electrical AC measurements with the exception that the measurements are acquired using wide frequency range instead of a single frequency. EIS have been used in concrete resistivity assessment [47], chloride monitor-

ing [18], evaluating reinforcing bar corrosion [11–14, 101], assessment of moisture and drying in cover zone concrete [16, 54] and fiber dispersion assessment [6, 8, 9]. Although electrical resistivity and impedance spectroscopy measurements have been proven effective in determining various properties of concrete, the drawback is that the methods are sensitive to uncertainties and inaccuracies of the models. Especially, the geometry of the target often cannot be modeled accurately. Moreover, the models in impedance spectroscopy do not take into account spatial variations of concrete conductivity.

Tomographic modalities based on electrical measurements are emerging methods for NDT of concrete. One potential modality is electrical resistance tomography (ERT), in which the objective is to reconstruct the internal 3D resistivity (or its reciprocal, conductivity) map from boundary voltage measurements. In 1994, Daily et. al. [36] applied ERT to image reinforced concrete. However, the quality of the reconstructions was not sufficient for practical applications. Buettner et. al. [37, 38] performed water infiltration tests, which demonstrated that ERT can be used for monitoring the temporal evolution of moisture distribution in concrete structures. More recently, Hou and Lynch [39] showed that ERT is applicable for detection of cracks in fiber-reinforced cement composites. In the paper by Hou and Lynch, the results were computed using a reference conductivity map of an intact sample before cracking. This approach was adopted to remove inhomogeneities from the reconstructions. However, when imaging existing concrete structures, the reference conductivity map of the pre-cracked target is usually not available, and hence the reconstructions should be solely based on the measurements acquired after a (possible) damage. A more detailed discussion on the method is given in Chapter 4. The feasibility of the method for imaging concrete, localizing rebars and detecting cracks is discussed in Chapter 5.

# 4 Electrical Resistance Tomography

Electrical resistance tomography (ERT) is an imaging modality in which the internal conductivity (or resistivity) distribution of the target is reconstructed on the basis of boundary voltage measurements. The challenge of image reconstruction in ERT is that the problem is an *ill-posed inverse problem*. This means that the solution is non-unique and extremely sensitive to measurement noise and modeling errors. As a consequence, accurate measurements and mathematical models as well as additional information about the target are needed in order to solve the problem. In this chapter, the practical aspects of ERT such as data acquisition, the computational models and the image reconstruction based on Bayesian framework are reviewed.

## 4.1 BACKGROUND

Electrical resistance tomography (ERT) is a noninvasive imaging method used in medical, geophysical and industrial applications. The history of ERT closely links back to the initiation of electrical impedance tomography (EIT)[1] in 1978 when two papers considering an "impedance camera" were published independently by Henderson and Webster [102] for medical imaging and by Lytle and Dines [103] for geophysical imaging. The research in both the theoretical and practical aspects of ERT started in 1980 when Calderón formulated the mathematical problem of recovering the internal conductivity distribution from boundary voltage measurements [104]. The most well known works in the theoretical field are the solution to the Calderón's problem in dimension three and higher for smooth conductivities by Sylvester and Uhlmann [105] and in dimension two for conductivities with two derivatives by Nachman [106]. The Calderón's original conjecture in dimension two was proved by Astala and Päivärinta in 2003 [107]. The first practical application of medical ERT was presented four years after the Calderón's original paper by Barber and Brown [108]. The potential applications of ERT are numerous. For example, the technique has been applied in biomedicine [27–31],

[1] The term EIT refers to imaging of the complex valued *admittivity* distribution based on full amplitude/phase angle data. However, it has been common to (slightly misleadingly) use the term EIT also when using the amplitude data only.

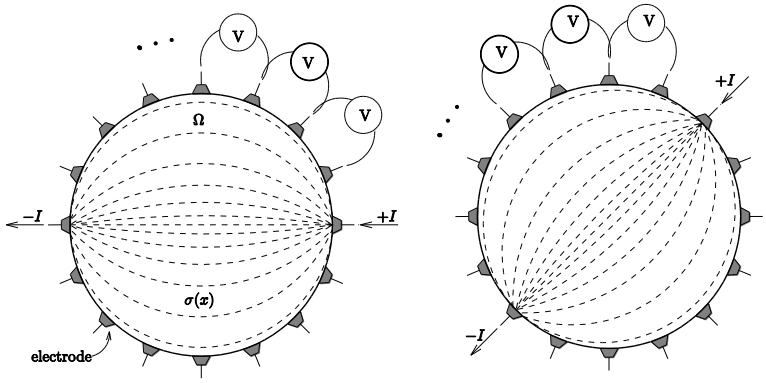


*Figure 4.1: Voltage measurements in ERT corresponding to two current injections.*

geology [32–34, 109], industrial process monitoring [110–114] and non-destructive testing [35,39]. In NDT, the potential applications include, for example, monitoring of water movement and temporal evolution of moisture distributions in concrete structures [37, 38, 115] and in identification of cracks [116,117]. For general reviews on ERT, see [21,118].

In ERT, electrical surface measurements are used to reconstruct the three-dimensional distribution of resistivity (or its reciprocal, conductivity) inside the target. An array of electrodes is attached on the surface and low frequency alternating currents are injected into the target through the electrodes. The resulting voltages are measured between several electrode pairs. The internal conductivity distribution is computed based on a set of voltage measurements corresponding to various current injection patterns. An example of the measurement strategy in ERT is shown in Figure 4.1.

ERT belongs to the class of *diffuse* tomography modalities. In diffuse tomography, the aim is to estimate the coefficients of a partial differential equation (PDE) based on noisy boundary measurements. ERT is a diffusive modality, because if a current is injected into the target volume between any two points, the electric current (density) spreads into the whole volume. As a consequence the image reconstruction is more complicated than, for example, in X-ray tomography, in which the rays travel in straight lines and one measurement carries information from a very restricted subset of the target. The image reconstruction problem in diffuse tomography has a nature of an *ill-posed inverse problem*. The practical definition of ill-posed inverse problems is that even moderately small

measurement and modeling errors can cause large errors in the solution. More precisely, the ill-posedness implies that classical (*least squares* (LS)) solutions are unstable and nonunique.

The first attempts to reconstruct an ERT image were based on the filtered back projection method (FBP) [108,119]. The FBP method is based on a coarse *ad hoc* -model of the electrical conduction in a medium. Thus, the quality of reconstructions obtained with the FBP method is inferior to those obtained with more sophisticated techniques. However, the FBP method is relatively fast and, despite the low quality of reconstructions, still widely in use.

A more versatile approach is to construct a "physically sound" model, or an electrode model, for the observations. A few electrode models for ERT exists, such as *continuum model*, *gap model*, *shunt model* and *complete electrode model* [120,121]. Although using an appropriate electrode model is superior to FBP method, the drawback is that the inverse problem becomes more challenging. A traditional approach to solve the ERT inverse problem based on an electrode model is the *Tikhonov regularization* [122]. In Tikhonov regularization the classical LS-problem is augmented with a regularizing penalty functional. The idea of the regularizing penalty functional is to stabilize the inverse problem by replacing the original ill-posed problem by a well-posed approximation that (hopefully) is close to the original one.

An alternative approach for treating the ERT inverse problem is statistical (Bayesian) inversion [22,41]. In the Bayesian approach, the problem is to estimate the posterior probability density of the unknowns given the measurement data and the additional *a priori* information about the unknowns. The *a priori* information is incorporated into a form of *prior probability density* that is based on statistical analysis of the characteristics of the unknown quantities. The prior information improves the reliability of the estimates and makes it possible to take uncertainties in the mathematical models into account. The reconstruction methods used in this thesis are solely based on the Bayesian framework. The Bayesian approach for ERT is briefly considered in Section 4.4.

## 4.2 DATA ACQUISITION IN ERT

The measurement setting in ERT is to place the electrodes, usually metallic ones, on the boundary of the target. In the early era of ERT, when the computational models were two dimensional, the electrodes were placed

in one circular array around the target. In three dimensional ERT there is more variation for electrode placement. Often, it is advisory to use the electrodes to cover all accessible parts of the surface around the region of interest. In this thesis, for example, ERT measurements were acquired from (real world) 3D cases in slab-like geometries in which the opposite surface is not always available for measurements. In such cases, the electrodes have to be placed on one of the (planar) surfaces. In some cases, the electrodes can also be placed *inside* the target [123, 124].

Most of the ERT systems are designed such that they inject currents and measure voltages instead of applying voltages and measuring currents [125]. This is due to the fact that there always exists a contact impedance between the electrode and the target complicating the ERT measurements. The contact impedances have a negligible effect on the voltage measurements when the current injection through the measurement electrodes is off. On the other hand, the contact impedances have their biggest effect on ERT reconstructions when the voltages are measured from current carrying electrodes. The traditional remedy has been to discard these measurements. However, it has been shown in [126] that the measurements from the current carrying electrodes have the best information content about the conductivity distribution. In this thesis, the contact impedances are taken into account by estimating them simultaneously with the conductivity distribution. When the contact impedances are known (estimated), the full voltage measurement data can be exploited in the ERT reconstructions.

Several ERT measurement systems exist, see e.g. [114, 127–129]. A typical ERT measurement device provides alternating currents between $1 - 100$ kHz. The AC current injections are preferred over DC to prevent the electrodes from polarizing. The currents are injected into the target through the electrodes for a period that it takes to record the corresponding (alternating) voltages. A normal procedure is to record only the (RMS) amplitudes and leave the phase shift information out from the measurement data. A standard method to collect the data is to measure the electrode voltages with respect to some reference electrode. The reference electrode can be either fixed or it can be changed for each measurement.

The current injection strategies in ERT can be divided in two main classes, which are known as *pair* and *multiple drive methods*. In pair drive methods the current is driven into the object through a pair of electrodes and the voltages are measured using all the electrodes. The most widely used selections for the pairwise current injection in circular geometry are *adjacent injection* and *opposite injection*, see e.g. [130]. In the multiple drive

methods, all electrodes can be used for simultaneous current injection. As a drawback, an individual current generator is required for each electrode increasing the complexity of the measurement system. However, this method usually yields a more uniform current density within the object, which often results in a better sensitivity [126]. For example, the most widely used multiple drive current injection strategy that produces a good overall sensitivity, is obtained by using the *trigonometric current patterns* [131, 132]. For Bayesian approach to optimizing current patterns, see [133, 134].

## 4.3 MEASUREMENT MODEL

The inverse problem of ERT is to reconstruct the internal conductivity distribution given the boundary voltages. In order to solve the inverse problem, a mathematical model (i.e. *forward model*) that describes the measurements is needed. The most accurate model so far is known as the *complete electrode model* (CEM).

### 4.3.1 Complete electrode model

The derivation of the CEM for ERT is based on the Maxwell's equations of electromagnetism in linear and isotropic continuous medium. With the assumptions that the capacitive and magnetic effects can be neglected, the Maxwell's equations inside a domain $\Omega \subset \mathbb{R}^3$ yield to Poisson equation [121]:

$$\nabla \cdot (\sigma(x)\nabla u(x)) = 0, \quad x \in \Omega. \tag{4.1}$$

In equation (4.1), $x$ is a (three dimensional) position vector in the domain $\Omega$, the function $\sigma(x)$ is the electrical conductivity of the medium and $u(x)$ is a (scalar) electric potential inside the domain. Generally, this approximation is considered accurate enough when the frequency of the alternating electric field is low. The equation (4.1) is known as the *quasi-static approximation*.

The complete electrode model consists of the partial differential equa-

tion equation (4.1) and the following boundary conditions

$$\int_{e_\ell} \sigma(x) \frac{\partial u(x)}{\partial \bar{n}} \, dS = I_\ell, \quad \ell = 1, \ldots, N_{el} \tag{4.2}$$

$$u(x) + z_\ell \sigma(x) \frac{\partial u(x)}{\partial \bar{n}} = U_\ell, \quad x \in \partial\Omega, \; \ell = 1, \ldots, N_{el} \tag{4.3}$$

$$\sigma(x) \frac{\partial u(x)}{\partial \bar{n}} = 0, \quad x \in \partial\Omega \setminus \bigcup_{\ell=1}^{N_{el}} e_\ell \tag{4.4}$$

where $U_\ell$ is the (RMS) potential on $\ell^{\text{th}}$ electrode, $I_\ell$ denotes the RMS of the electric current applied through the electrode $e_\ell$, $z_\ell$ is the contact impedance (resistance) between the $\ell^{\text{th}}$ electrode and the domain $\Omega$, and $\bar{n}$ is the unit normal pointing outward from the boundary $\partial\Omega$. The boundary conditions (4.2)–(4.4) can be interpreted as follows: The condition (4.2) fixes the total current through $\ell^{\text{th}}$ electrode to the injected current $I_\ell$. The condition (4.3) takes into account the constant potential on the electrodes (i.e. *shunting effect*) and the contact impedance between the electrodes and the medium. The last condition states that the current through the electrode-free part of the boundary is zero. In addition to boundary conditions (4.2) – (4.4), the charge conservation law has to be obeyed. Thus, it is required that

$$\sum_{\ell=1}^{N_{el}} I_\ell = 0, \tag{4.5}$$

where $\ell = 1, \ldots, N_{el}$. Further, the potential reference level needs to be fixed, for example, by writing

$$\sum_{\ell=1}^{N_{el}} U_\ell = 0. \tag{4.6}$$

This electrode model was first proposed in [120], and the existence and uniqueness of the forward problem was discussed in [121].

### 4.3.2 Finite element approximation of CEM

The complete electrode model (4.1) – (4.4) relates the electrode potentials $U_\ell$, the injected currents $I_\ell$ and the conductivity distribution $\sigma$ together. The forward problem in ERT is to solve the internal electric potential $u(x)$ and the electrode potentials $U_\ell$, when the conductivity and the injected currents are given. The analytical solution of the CEM is possible only for very simplified cases due to the rather complicated boundary conditions.

Therefore, one has to employ some numerical methods in order to tackle the problem. In this section, a finite element approximation for the CEM is briefly reviewed. For a more thorough derivation of the variational form, see [121]. For the finite element formulation of the CEM in 2D and 3D, see [135] and [136,137], respectively.

In the finite element method (FEM), the domain $\Omega$ is divided into a mesh of finite number of elements and the solution $u(x)$ for the problem (4.1) – (4.6) is approximated in this mesh as a finite dimensional approximation $u_h \approx u(x)$ of the form

$$u_h = \sum_{i=1}^{N} u_i \varphi_i(x), \quad x \in \Omega \tag{4.7}$$

where N is the number of nodes in the finite element mesh. In this thesis, the basis functions $\varphi_i(x)$ are piecewise polynomial (first or higher order) chosen such that the coefficients $u_i$ give the finite element solution $u_h$ in the nodal points. For the electrode potentials $U_\ell$ and internal conductivity $\sigma(x)$, the following approximations $U_\ell \approx U_h$ and $\sigma(x) \approx \sigma_h$ are chosen, such that

$$U_h = \sum_{j=1}^{Nel-1} \tilde{u}_j n_j, \quad n_j \in \mathbb{R}^{Nel} \tag{4.8}$$

$$\sigma_h = \sum_{j=1}^{N} \sigma_j \phi_j(x), \tag{4.9}$$

where $n_j$ are constant vectors chosen such that the condition (4.6) holds, e.g. $n_j = (1, 0, \ldots, -1, 0, \ldots, 0)^T$, where the $(j+1)^{\text{th}}$ component is $-1$. Further, $\tilde{u}_j$ are the associated coefficients. In this thesis, the basis functions $\phi_j(x)$ are piecewise first order polynomials and $\sigma_j$ is the associated coefficient for the $j^{\text{th}}$ basis function $\phi_j$. In the sequel, the conductivity distribution $\sigma(x)$ is identified by the coefficient vector $\sigma = (\sigma_1, \ldots, \sigma_N)^T \in \mathbb{R}^N$.

The finite element approximation of the CEM can be written as a matrix equation

$$A\bar{u} = f, \tag{4.10}$$

where $A$ is the FEM system matrix [135], $\bar{u}^T = (\bar{u}_1^T, \bar{u}_2^T)$ is the solution vector that holds the coefficients of the equations (4.7) and (4.8) in the vectors $\bar{u}_1 = (u_1, \ldots, u_N)^T$ and $\bar{u}_2 = (\tilde{u}_1, \ldots, \tilde{u}_{N_{el}-1})^T$. The data vector $f \in \mathbb{R}^{N+N_{el}}$ is constructed such that

$$f = \begin{pmatrix} \bar{0} \\ \mathcal{C}^T I \end{pmatrix},$$

where $\bar{0} = (0, \ldots, 0)^T \in \mathbb{R}^N$, $I \in \mathbb{R}^{N_{el}}$ is the injected current and $\mathcal{C} = (n_1, \ldots, n_{N_{el}-1}) \in \mathbb{R}^{N_{el} \times N_{el}-1}$.

An approximative solution for the forward problem is obtained by solving the equation (4.10) as $\bar{u} = A^{-1}f$. The potentials $U_h$ on the electrodes can be computed by using the equation (4.8), that is in the matrix form as $U_h = \mathcal{C}\bar{u}_2$. Thus, the relation between the injected currents $I$ and the computed potentials on the electrodes can be written in the form

$$U_h = \mathcal{C}\bar{u}_2 = \mathcal{C}\tilde{\mathcal{R}}(\sigma, z)\mathcal{C}^T I = \mathcal{R}(\sigma, z)I, \tag{4.11}$$

where matrix $\tilde{\mathcal{R}}(\sigma, z) \in \mathbb{R}^{(N+N_{el}-1)\times(N+N_{el}-1)}$ is a bottom right block of the inverse $A^{-1}$ of the FEM system matrix $A$. The matrix $\mathcal{R}(\sigma, z)$ is referred to as the *resistance matrix*.

In practice, the actual measurements in ERT are voltages measured between selected electrode pairs, that is $\mathcal{V}_i = U_l - U_k$, $i = 1, \ldots, m$, where $m$ is the number of measurements. For example, the voltage measurement vector $\mathcal{V}$ may consist of potential differences $\mathcal{V}_1 = U_2 - U_1$, $\mathcal{V}_2 = U_3 - U_2$, etc. In matrix form, the measurements can be written as

$$\mathcal{V} = \mathcal{M}U_h$$

where $\mathcal{M} \in \mathbb{R}^{m \times N_{el}}$ is called the *measurement matrix*.

Next, consider an ERT measurement with multiple current injections and assume that the ERT voltage measurements $\mathcal{V}$ are contamined with additive noise $e$. Then the observations, the unknowns and the measurement noise are tied together through an *additive observation model* of ERT that is of the form

$$\begin{pmatrix} \mathcal{V}(I_1) \\ \vdots \\ \mathcal{V}(I_p) \end{pmatrix} = \begin{pmatrix} \mathcal{M}\mathcal{R}(\sigma, z)I_1 \\ \vdots \\ \mathcal{M}\mathcal{R}(\sigma, z)I_p \end{pmatrix} + \begin{pmatrix} e_1 \\ \vdots \\ e_p \end{pmatrix}, \tag{4.12}$$

where the observations are stacked for $p$ current injections $I_1, I_2, \ldots, I_p$. Equation (4.12) can be written more shortly as

$$V = R(\sigma, z) + e, \tag{4.13}$$

where $V \in \mathbb{R}^{pN_{el}}$ corresponds now to a full ERT measurement with observed voltages for $p$ injected currents and $e = (e_1^T, \ldots, e_p^T)^T$. Note, however, that the disturbances in industry can have various different noise characteristics and the additive noise model is not always adequate. More complicated noise models are studied, for example, in [41].

## 4.4 A BAYESIAN APPROACH TO ERT

In previous sections the forward problem in ERT was discussed. The forward problem is to compute the electrode potentials when the conductivity distribution and the contact impedances are known. The inverse problem, on the other hand, is to reconstruct the conductivity distribution based on noisy electrode potential differences. The ERT inverse problem is ill-posed and highly nonlinear and thus sophisticated inversion methods are needed in order to solve the problem. In this section, a statistical approach based on the Bayesian framework for solving the ERT inverse problem is briefly discussed. For a more comprehensive discussion on this topic, see e.g. [22,40,41]. As a general reference to probability theory, see e.g. [138].

In statistical inverse problems all variables are considered as random variables. The randomness is thought to reflect our incomplete information about the unknown variables. The information about the unknown variables is expressed as probability densities called *prior densities*, e.g. $\sigma \mapsto \pi_{\mathrm{pr}}(\sigma)$. As the name suggests, the prior density holds the information we know about the parameter of interest prior to the measurement. The complete solution of the inverse problem in Bayesian framework is the *posterior distribution* $\pi(\sigma, z|V)$, i.e. the conditional probability distribution of $\sigma$ and $z$ given the observations $V$.

The posterior density is given by the *Bayes formula* that can be written for ERT as

$$\pi(\sigma, z|V) = \frac{\pi(V|\sigma, z)\pi_{\mathrm{pr}}(\sigma, z)}{\pi(V)}, \tag{4.14}$$

where $\pi(V|\sigma, z)$ is the *likelihood density* or *likelihood model*, $\pi(V)$ is a marginal density which mainly acts as normalization constant and $\pi_{\mathrm{pr}}(\sigma, z)$ is the joint prior density of conductivity $\sigma$ and contact impedances $z$. The normalization constant can often be neglected and the equation (4.14) simplifies to the form

$$\pi(\sigma, z|V) \propto \pi(V|\sigma, z)\pi_{\mathrm{pr}}(\sigma, z). \tag{4.15}$$

The likelihood density is a conditional density of the observations given the unknowns and thus describes their mutual relation based on the observation model. If we assume that the unknowns $(\sigma, z)$ and the additive measurement noise in equation (4.13) are mutually independent, the likelihood can be written as [139]:

$$\pi(V|\sigma, z) = \pi_e(V - R(\sigma, z)), \tag{4.16}$$

where $\pi_e$ is the probability density of the noise $e$. Further, if the measurement noise $e$ is Gaussian distributed with zero mean and covariance $\Gamma_e$, the likelihood takes the form

$$\pi(V|\sigma, z) \propto \exp\left(-\frac{1}{2}(V - R(\sigma, z))^T \Gamma_e^{-1}(V - R(\sigma, z))\right). \tag{4.17}$$

Furthermore, assume that $\sigma$ and $z$ are modelled as mutually independent, that is $\pi_{\text{pr}}(\sigma, z) = \pi(\sigma)\pi(z)$. If the corresponding prior models are Gaussian distributions, such that

$$\pi(\sigma) \propto \exp\left(-\frac{1}{2}(\sigma - \sigma_*)^T \Gamma_\sigma^{-1}(\sigma - \sigma_*)\right), \tag{4.18}$$

$$\pi(z) \propto \exp\left(-\frac{1}{2}(z - z_*)^T \Gamma_z^{-1}(z - z_*)\right), \tag{4.19}$$

where $\sigma_*$ and $z_*$ are the means of conductivity and contact impedances, $\Gamma_\sigma$ and $\Gamma_z$ being the covariance matrices, then the posterior density (4.15) can be written as [41, 140]

$$\begin{aligned}\pi(\sigma, z|V) \propto \exp\Bigg(&-\frac{1}{2}(V - R(\sigma, z))^T \Gamma_e^{-1}(V - R(\sigma, z)) \\ &-\frac{1}{2}(\sigma - \sigma_*)^T \Gamma_\sigma^{-1}(\sigma - \sigma_*) \\ &-\frac{1}{2}(z - z_*)^T \Gamma_z^{-1}(z - z_*)\Bigg).\end{aligned} \tag{4.20}$$

Although the posterior density in equation (4.20) is formally the solution of the statistical inverse problem, in high dimensional problems it alone is impractical for direct interpretation and visualization of the solution. Usually some *point and interval or spread estimates* are computed from the posterior distribution.

One of the most employed statistical point estimates is the *maximum a posteriori* (MAP) estimate

$$(\sigma, z)_{\text{MAP}} = \arg\max_{(\sigma,z)} \pi(\sigma, z|V), \tag{4.21}$$

which gives the maximum point of the posterior density. With the assumptions give above, the computation of the MAP-estimate yields the minimization of the (negative) exponent in (4.20), that is

$$(\sigma, z)_{\text{MAP}} = \arg\min_{(\sigma,z)} F(\sigma, z; V), \tag{4.22}$$

where the functional $F(\sigma, z; V)$ is of the form

$$\begin{aligned} F(\sigma, z; V) &= (V - R(\sigma, z))^T \Gamma_e^{-1} (V - R(\sigma, z)) \\ &\quad + (\sigma - \sigma_*)^T \Gamma_\sigma^{-1} (\sigma - \sigma_*) + (z - z_*)^T \Gamma_z^{-1} (z - z_*) \\ &= \|L_e(V - R(\sigma, z))\|^2 \\ &\quad + \|L_\sigma(\sigma - \sigma_*)\|^2 + \|L_z(z - z_*)\|^2 \end{aligned} \tag{4.23}$$

and where $L_e$, $L_\sigma$ and $L_z$ are the Cholesky factors of covariance matrices such that

$$\Gamma_e^{-1} = L_e^T L_e, \quad \Gamma_\sigma^{-1} = L_\sigma^T L_\sigma \quad \text{and} \quad \Gamma_z^{-1} = L_z^T L_z. \tag{4.24}$$

An interesting property of the MAP-estimate is that with the Gaussian assumptions given above about the unknowns $(\sigma, z)$ and measurement noise $e$, the functional (4.23) is equivalent to classical (generalized) *Tikhonov regularized* functional [122]. Tikhonov regularization has been widely used in inverse problems. Note, however, that in Tikhonov regularization the interpretation of the functional (4.23) and construction of $L_\sigma$ and $L_z$ are totally different from those in statistical inversion.

Since the functional (4.23) is nonlinear, the computation of the MAP-estimate (4.22) leads to *nonlinear minimization problem*. The minimizer is typically found using gradient based iterative techniques such as Gauss-Newton (GN) method [141, 142]. Consider next a GN iteration step, in which a parenthesized super-index is used to refer an iteration number, and let $\xi = (\sigma^T, z^T)^T$ be a vector that denotes the unknowns. Now, in the case of problem (4.22) with the initial value $\xi_0$ fixed, the iteration step $\xi^{(i+1)}$, $i \geq 0$ is computed as follows

$$\xi^{(i+1)} = \xi^{(i)} + \lambda^{(i)} \delta_\xi^{(i)}, \tag{4.25}$$

where the parameter $\lambda^{(i)}$ controls the step size in the search direction $\delta_\xi^{(i)}$, which in turn is given by the formula [139]

$$\begin{aligned} \delta_\xi^{(i)} = &\left( (J^{(i)})^T \Gamma_e^{-1} J^{(i)} + \Gamma_\xi^{-1} \right)^{-1} \\ &\cdot \left( (J^{(i)})^T \Gamma_e^{-1} (V - R(\xi^{(i)})) - \Gamma_\xi^{-1} (\xi^{(i)} - \xi_*) \right), \end{aligned} \tag{4.26}$$

where $\Gamma_\xi = \operatorname{diag}(\Gamma_\sigma, \Gamma_z)$ is the block diagonal covariance matrix of the (total) unknown vector $\xi$ and $\xi_* = (\sigma_*^T, z_*^T)^T$ is the mean. Often, the initial value is set as $\xi_0 = \xi_*$. In equation (4.26), the term $J^{(i)}$ is the Jacobian

matrix of the forward mapping $\xi^{(i)} \mapsto R(\xi^{(i)})$ expressed in a form of a block matrix, such that $J^{(i)} = (J_\sigma, J_z)$, where the block matrices are

$$J_\sigma = \left.\frac{\partial R(\sigma, z)}{\partial \sigma}\right|_{(\sigma^{(i)}, z^{(i)})}, \qquad J_z = \left.\frac{\partial R(\sigma, z)}{\partial z}\right|_{(\sigma^{(i)}, z^{(i)})},$$

where $\sigma^{(i)}$ and $z^{(i)}$ are defined as $({\sigma^{(i)}}^T, {z^{(i)}}^T)^T = \xi^{(i)}$. The computation of the Jacobian blocks $J_\sigma$ and $J_z$ are presented in references [137] and [143], respectively. In this thesis, all the results were obtained by computing the MAP-estimate using the Gauss-Newton (GN) method equipped with a line search and positivity constraints. For more details on the applied GN-method and other optimization methods in ERT, see for example [137].

The MAP-estimate is often the best choice when aiming at computationally effective methods. There exists also other popular point estimates, such as *conditional mean* (CM) estimate and *maximum likelihood* (ML) estimate. The computation of the CM-estimate is a (high dimensional) integration problem and often Markov chain Monte Carlo (MCMC) techniques have to be used, which are computationally demanding. The ML-estimate gives the maximum point of the likelihood density, and it corresponds to the solution of non-regularized inverse problem. Thus, in the case of ill-posed inverse problems the ML-estimate is unstable. For more information on point estimates in statistical inversion, see e.g. [22,41,140].

In the Bayesian framework, the most crucial step is the selection of the prior density. For the prior models, there are several possibilities, such as the classical white noise model, *(improper) smoothness priors* [144], *proper smoothness priors* [41], *inhomogeneous and anisotropic (structural) smoothness priors* [145], *total variation priors* [22,146], $L^1$ *(impulse) priors* [22,147], and *Besov priors* [148]. The selection of the prior model is based on the prior information and the assumptions on the target as well as the required computational complexity of the method. For example, targets that are results of diffusion processes, are usually modeled as (homogeneous) smoothness processes, while targets, which have small objects embedded in relatively homogeneous background, might be modeled with an $L^1$ prior model.

The most common prior models in ERT are the smoothness priors [149–152], which favor (spatially) smooth solutions. In these cases, the Cholesky factor of the prior covariance (see eq. (4.24)) is typically a discrete approximation of some differential operator. A more versatile prior can be obtained by employing the (*inhomogeneous*) *anisotropic smoothness prior* [145]. In this prior, uneven smoothness assumption in different directions can be taken into account. Anisotropic smoothness prior is a versatile concept that can be used in many cases in which we have prior

information about the orientation of internal structures. In this thesis, for example, the anisotropic smoothness prior was exploited in most of the cases considering rebars and cracks in concrete.

# 5 ERT imaging of concrete

In this chapter, the feasibility of electrical resistance tomography for imaging concrete is discussed and the results obtained in Publications **I – IV** are outlined.

The discussion begins in Section 5.1 with a brief review of the employed measurement systems and strategies in this thesis. The feasibility of ERT for imaging various embedded targets in concrete was studied in **I**, and the main findings are presented in Section 5.2. The applicability of ERT to identification of cracks in concrete was studied in **II**. In **IV**, a novel computational method was developed for more accurate crack identification. The publications **II** and **IV** are reviewed in Section 5.3. In section 5.4, the localization of rebars using a novel numerical scheme for ERT is discussed based on **III**.

## 5.1 INSTRUMENTATION

In this thesis, two instruments for ERT measurements were mainly used: Kuopio impedance tomography (KIT4) device developed in University of Eastern Finland in Kuopio [114], and Radic Research SIPFIN instrument.[1] Both instruments are capable of injecting alternating currents and measuring the resulting alternating voltage data. In this thesis the phase information was neglected and only the (RMS) amplitude of the voltage data was used. The measurement frequencies were largely dictated by the measurement devices and varied between 1 Hz to 1 kHz. Thus, the measurements were operated within the pure resistive region of the concrete (see Section 2.2).

In electrical measurements of concrete, obtaining a good contact with the concrete surface is important. In this thesis, two different electrode types were considered, namely, *wet electrodes* and *gel electrodes*. In **I**, wet electrodes were developed for ERT imaging of concrete. The wet electrodes are copper-copper sulphate (Cu-$CuSO_4$) electrodes, with similar construction to those described by Monteiro et al. [11]. With Cu-$CuSO_4$ electrodes, the electrical contact is obtained by attaching a wet sponge to

[1] SIPFIN is based on a Radic Research SIP256 instrument with slight modifications to concrete ERT. For more information on SIP256, see `http://www.radic-research.de`

the concrete surface. The sponge is wetted with copper sulphate solution, which is stored inside a hollow copper cylinder covered by a plastic casing. The current and voltage leads to ERT instrument are connected to the copper cylinders. The electrodes are pushed towards the concrete surface with springs. The advantages of using Cu-$CuSO_4$ electrodes are: (1) the wet sponge ensures a sufficient electrical contact to concrete, and (2) the polarization between copper and copper sulphate is low. One of the electrodes is shown in publication **I**, Figure 3a.

When using wet Cu-$CuSO_4$ electrodes for measuring concrete, the copper sulphate solution is absorbed through the concrete surface. When imaging dry concrete, the continuous absorption of the solution can cause ERT measurements to become less sensitive to concrete properties because: 1) the contact impedances between the electrodes and concrete may change during the measurements; and 2) if the electrode array is small, the absorbed solution may form conductive paths between the neighboring electrodes.

The gel electrodes employed in publication **II** were steel electrodes with non-polarizing electrode gel used between the steel and concrete. The gel electrodes were found to be more stable than Cu-$CuSO_4$ electrodes because by using gel electrodes most of the absorption problems with wet electrodes can be avoided. Hence, the gel electrodes were preferred over the wet electrodes in later experiments, even though the contact is sometimes slightly worse than with the wet electrodes.

## 5.2 FEASIBILITY OF ERT FOR IMAGING CONCRETE

The feasibility of ERT to 3D imaging of concrete was studied in **I**. Several specimens with different types of inclusions were prepared. In reality, the electrical conductivity distribution of concrete is not characterized by a uniform background conductivity and the embedded inclusions alone, but moisture and chloride gradients, for example, also induce a significant conductivity gradient. Furthermore, as pointed out in Chapter 2, concrete is a highly heterogeneous material containing large and small aggregate particles, hardened cement paste and air voids. In this feasibility assessment, however, the investigation concerns only on how well structural inhomogeneities such as rebars and cracks can be detected from a more or less uniformly conducting background.

### 5.2.1 Experimental results

Short cylindrical specimens were cast (15 cm in diameter, 3 cm high). Concrete had the following mixture proportion: aggregates (83 %), Portland cement (15 %), and fly ash (2 %) by mass. The maximum size of the aggregate was 8 mm and the $w/c$ ratio of 0.8 was used, resulting in a compressive strength of 20-25 MPa. The following cases are considered:

**Case 1:** Concrete specimen with resistive inclusion (block) made of polyurethane foam.

**Case 2:** Concrete specimen with conductive steel bars.

**Case 3:** Specimens with different crack sizes.

The measurements were carried out using KIT4 instrument nine days after the concrete specimens were casted. In all cases, the MAP-estimate (4.21) with anisotropic smoothness prior model was computed following the scheme described in Section 4. The reconstruction software (including the FE package for forward computations) is an adaption of the implementations described in [136, 143, 145, 153, 154]. For further information about the specimens, measurements and reconstruction techniques, see publication **I**.

The results are shown in Figures 5.1– 5.3. The first specimen with an embedded polyurethane block and a surface plot of the corresponding conductivity reconstruction are shown in Figure 5.1. The block was positioned off-center in the horizontal plane, and placed vertically through the concrete cylinder. The conductivity reconstruction shows clearly an insulating region at the location of the polyurethane block. Because the insulating polyurethane block corresponds closely to a large air void, the imaging of such resistive voids could be possible.

In Figure 5.2, the specimens with embedded steel bars (case 2) are shown. The first specimen contains a vertically oriented steel bar (diameter 3 cm) approximately in the same location as that of the polyurethane block in case 1. The second specimen contains a horizontally oriented steel bar (diameter 1 cm, length 7 cm) that is not visible from outside. In the reconstructions, anisotropic smoothness prior with logarithmic parametrization was used. This prior yields conductivity distributions that are smooth in the logarithmic scale and thus allow for variations of several orders of magnitude for the conductivity [155, 156]. In the first case, no assumptions about the orientation of the steel bar were made and the smoothness was set equal to every direction. In the second case, the orientation of the bar was assumed to be approximately known. Thus, the anisotropic

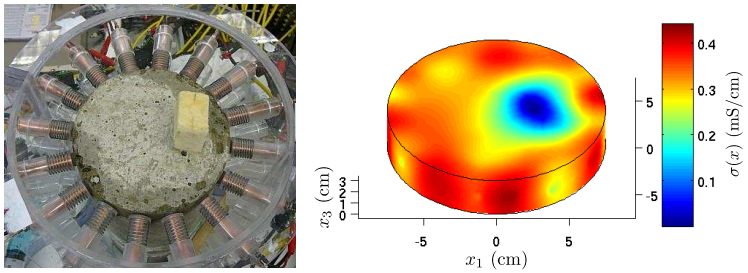


*Figure 5.1: Results for the experimental case 1: a specimen with embedded polyurethane block (left) and the corresponding conductivity reconstruction (right).*

smoothness prior was employed with high smoothness in the direction of the steel bar. In both cases, the contrast between the reconstructed conductivities of the steel and concrete is high.

The results for the specimens with cracks (case 3) are shown in Figure 5.3. In the first two of these experiments, thin transparent sheets (widths 6 cm and 3 cm) were cast inside the concrete specimens to simulate non-conductive cracks with different sizes. The difference between the crack sizes in the reconstructed images is clear. Further, the orientation and the actual size of both cracks are quite well reconstructed. In both cases the reconstructed conductivity of the transparencies was close to zero, which was to be expected because the transparencies acted as insulators.

In addition to specimens with plastic sheets, a cylindrical specimen with a real crack was studied in the conference paper [157]. The specimen was cast using the same concrete batch as in the previous experiment and measured four months later. During this period, the specimen was covered in plastic to prevent excessive drying. The specimen was broken with a hammer and then measured with KIT4 instrument using metallic gel electrodes. The employed reconstruction software was same as in the previous cases. The specimen and the corresponding conductivity reconstruction are shown at the bottom row in Figure 5.3. The reconstruction clearly reveals the three main cracks in the specimen.

### 5.2.2 Discussion

The reconstructions in Figures 5.1– 5.3 show that ERT is applicable for imaging concrete. The experiments verify that it is possible to detect different resistive and conductive objects inside cylindrical concrete specimens. The reconstructed background conductivities, i.e. the conductivity

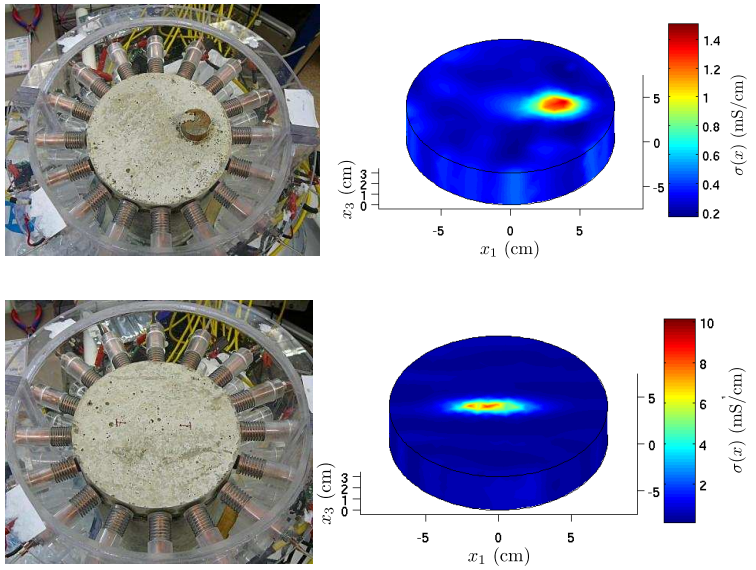


*Figure 5.2: Results for the experimental case 2. Top row: vertical steel bar in concrete (left) and the corresponding conductivity reconstruction (right). Bottom row: embedded (hidden) horizontal steel bar in the location indicated by red marks on the surface (left) and the corresponding reconstruction (right).*

of concrete, varies between 0.1 and 0.44 mS/cm, depending on the case. These values are within the range of conductivity of wet concrete as indicated in Table 2.1. The measured specimens were covered with plastic after casting and were thus relatively moist.

The conductivity reconstruction of the specimen with the polyurethane block correctly reveals an insulating region at the location of the block (Figure 5.1). However, the reconstruction of the background conductivity is not very homogeneous. The same feature is also noticeable in the case 3 for the specimens with transparencies (Figure 5.3, top and middle rows). Some of the inhomogeneities in the reconstruction may be imaging artefacts due to measurement and modeling errors; while others are related to the samples itself. The conductivity of concrete is never homogeneous: concrete is a mix of resistive aggregate particles in hydrated cement matrix, in which the free water in the porous system contributes for the conductivity of concrete. The main reason for the background conductivity variations here, however, is the fact the copper sulphate solution was absorbed by concrete from the wet electrodes. That is the reason for

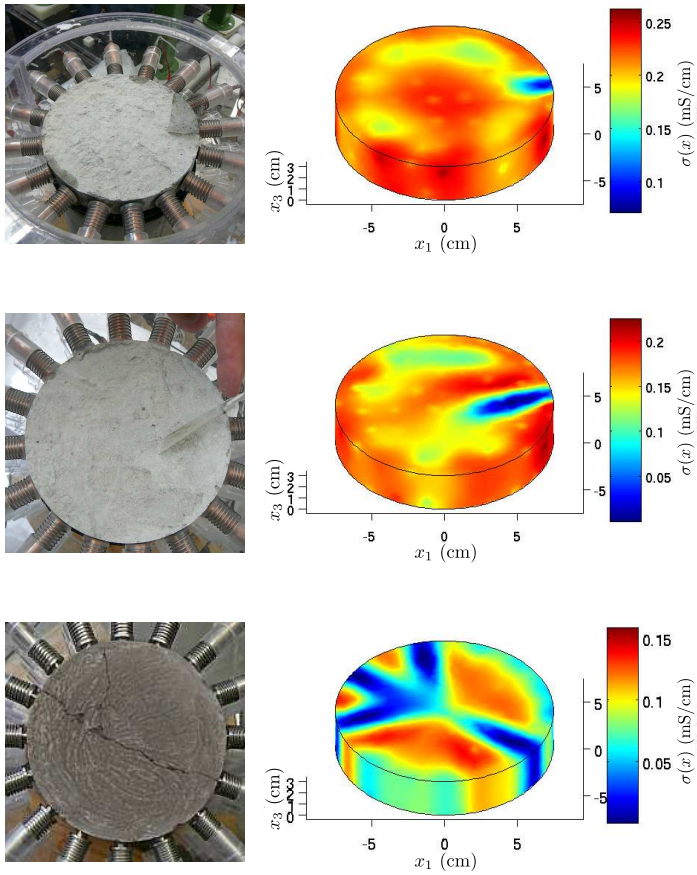


*Figure 5.3: Results for the experimental case 3. Top row: small plastic sheet embedded in concrete (left) and the corresponding conductivity reconstruction (right). Middle row: big plastic sheet embedded in concrete (left) and the reconstruction (right). Bottom row: the cracked concrete specimen (left) and the reconstruction (right).*

high conductivities on the measurement surface. This was verified by carrying out consecutive measurements cycles which showed an increase in the conductivities under the electrodes when more and more copper sulphate was absorbed. In the real crack case (Figure 5.3, bottom row), the high conductive areas in the neighborhood of the electrodes are not so frequently present. This is because of the use of gel electrodes. Although the gel (moistness) is also absorbed by concrete, the absorption is weaker than with the Cu-$CuSO_4$ electrodes.

In the case 2 (Figure 5.2), the steel bars are accurately localized with good contrast. Note, however, that the vertical coordinates of the horizontal bar (Figure 5.2, bottom row) cannot be localized using the data acquired in this experiment, because all the electrodes were placed on a single layer ($x_1x_2$-plane) and the measurement geometry thus is symmetrical with respect to this plane. The reconstructed concrete conductivity varies between 0.2 mS/cm and 0.6 mS/cm and appears more smooth than in the previous cases. This is because of the high contrast in conductivity between concrete and steel. Note, however, that the conductivity of the steel is in the range of $1 \cdot 10^5$ S/cm, which is significantly higher than the peak values 1.5 mS/cm and 10 mS/cm in Figure 5.2. The fact that conductivities of the steel bars are highly underestimated is a result of two effects: 1) the potential drop between the steel-concrete interface due to the contact impedance is not taken into account. 2) The boundary voltage measurements are not sensitive to conductivity contrast above some limit. This means that in a background of 0.2 mS/cm we are not necessarily able to distinguish between 2 mS/cm and 20 mS/cm inclusions. We are, however, able to detect a 20 mS/cm inclusion in a 2 mS/cm background.

The last experiment (Figure 5.3) demonstrates that it is possible to estimate cracks and the depth of cracks in concrete using ERT. The sizes of the two different transparencies are correctly identified in the reconstructions. In addition, the crack pattern in the broken specimen is reliably reconstructed. Although the specimen was first broken in distinct pieces (i.e. the most extreme form of cracking) and then assembled back together for measurements, the results confirm that at least major real cracks can be detected with ERT. All crack reconstructions here show resistive characteristics. Note, however, that real cracks can be either resistive or conductive depending on the moisture conditions [5].

## 5.3 CRACK DETECTION

In this section the detection of cracks in more realistic slab- and beam-like geometries using ERT is discussed. The discussion is based on the publications **II** and **IV**. The key idea in the papers was to continue the work started in **I** towards a crack detection in more realistic setup. In **II**, the applicability of ERT for crack detection in concrete slab and beam geometries was studied. The main findings of this study are reported in Section 5.3.1. In publication **IV**, the aim was to apply a novel computational approach for crack identification in solid materials. The results of this paper

are discussed in Section 5.3.2. The discussion on the results in **II** and **IV** is given in Section 5.3.3.

### 5.3.1 Applicability of ERT for crack detection

In publication **II**, the main focus was on investigating the capability of ERT for crack detection and characterization in slab and beam geometries in which the electrode array is attached to one planar surface of concrete. The geometries of that type are often more relevant in practice than the cylindrical geometries which allow measurements around the target.

#### Specimens

The experiments were carried out with six specimens: three slabs and three beams. With the slabs, the first aim was to investigate the ability of ERT to distinguish between different crack depths. The second aim was to study the feasibility of using ERT to detect laminar cracks. The feasibility of ERT for detection of real cracks was tested with the concrete beams. For this aim, the beams were cracked with three-point loading and the ERT measurements were acquired after cracking.

Three slab specimens with dimensions 50 cm $\times$ 50 cm $\times$ 4 cm were cast using concrete mix reported in Table 1, publication **II**. For each specimen, thin plastic sheets were embedded inside to simulate cracks with low conductivity. In the first two slabs, the plastic sheets were perpendicular to the concrete surface. The size of the first sheet was 40 mm in the depth direction whereas the corresponding size for the second sheet was 25 mm. In the third slab, the plastic sheet was placed parallel to the surface to model a case of laminar cracking (delamination). The sheet was set 10 mm below the measurement surface. The measurement setup and electrode configuration for the slabs are shown in **II**, Figures 2(a) and 3(a).

In the case of beam specimens, crack damages of three different magnitudes were induced to the beams (beam dimensions 8.9 cm $\times$ 11.4 cm $\times$ 40.6 cm): the first specimen was broken in two distinct pieces, the second specimen was three-point loaded until clearly visible crack (width $300 \pm 50$ $\mu$m on the measurement surface) appeared and the third specimen was three-point loaded until a very narrow crack (width $100 \pm 50$ $\mu$m) formed. The first specimen was also measured before cracking. The measurement setup and electrode configuration for the beams are shown in **II**, Figures 2(b) and 3(b). For more details on the concrete mixture

proportions, specimen details and computational aspects such as finite element discretizations and prior constructions, see **II**.

## Results

The results for the slab specimens are shown in Figure 5.4. The location and orientation of the plastic sheets are illustrated in the schematic figures on the left column. To visualize the reconstructed conductivity distributions, 3D surface plots were drawn in which the domain is cut from plane $x_1 = 26$ cm (right column). These midplane cross-section views reveal the volumes with low conductivity in the location of the plastic sheets. For the first two slabs (first and second row in Figure 5.4) the reconstructed sizes and shapes of the poorly conductive volumes match relatively well with those of the plastic sheets in the corresponding specimens (left column in Figure 5.4). The slab with a laminar plastic sheet and the corresponding reconstruction are shown on the last row in Figure 5.4. The reconstruction shows a large nonconductive sheet that is parallel with the top surface of the slab, indicating that laminar nonconductive cracks can be detected using ERT measurements from only one surface of the slab. However, the dimensions of the nonconductive volume are not equal to the dimensions of the plastic sheet. The dimensions of the nonconductive volume were approximately 400 mm $\times$ 200 mm $\times$ 20 mm, whereas the true dimensions of the plastic sheet were 190 mm $\times$ 140 mm $\times$ 2 mm as shown on bottom left in Figure 5.4. This dissimilarity between the real and estimated crack dimensions is discussed further in section 5.3.3.

Photographs and the conductivity reconstructions of the beam specimens are shown in Figure 5.5. The reconstruction of each specimen is illustrated with combined surface plots and cross section plots. All the reconstructions are represented in the same color scale. The top row in Figure 5.5 represent the first specimen before cracking and the second row (from the top) shows the same specimen after cracking. The difference between the reconstructions is very clear: the conductivity of the specimen before cracking is relatively homogeneous, whereas after cracking, a nonconductive region emerges in the location of the crack. Note, that both reconstructions were computed using exactly the same parameters. Note also, that the measurements obtained before crack were not utilized in the reconstruction of the beam conductivity after cracking. In the second specimen, an apparent crack induced in three-point loading vertically reached approximately the middle section of the beam. On the top surface, the width of the crack was approximately 300 $\mu$m ($\pm$50 $\mu$m).

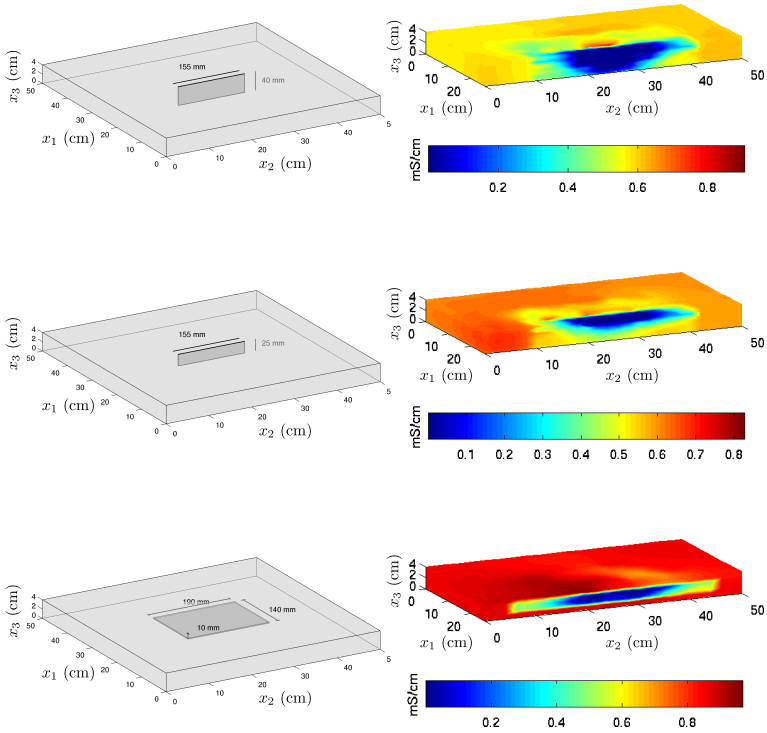


*Figure 5.4: Slab specimens (schematic representation on the left column) and the corresponding conductivity reconstructions (right column): 40 mm deep crack (top row), 25 mm deep crack (middle row) and laminar crack (bottom row).*

The size of the crack was visually estimated from photographs. The reconstruction of the second specimen is depicted right on the third row in Figure 5.5. The ERT reconstruction is in agreement with the visual inspection of the specimen; in the reconstruction, a nonconductive region reaching from the top surface to middle of the beam was detected. The left image on the bottom row in Figure 5.5 shows the top surface of the third specimen with a very narrow crack. On the top surface, the width of the crack was approximately 100 $\mu$m ($\pm$50 $\mu$m). The ERT reconstruction reveals a region with lower conductivity near to the beam surface. However, in this case the reconstructed conductivity distribution has less contrast between the background and crack area.

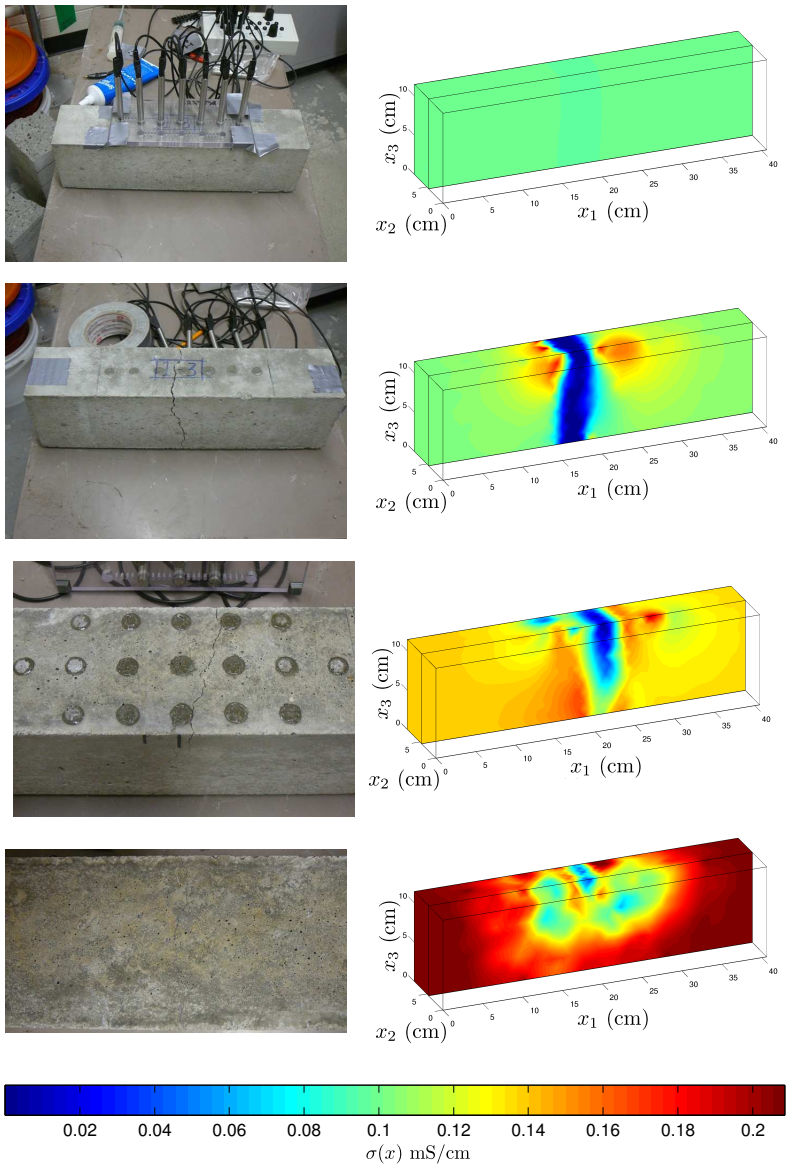


*Figure 5.5: Beam specimens (left column) and the corresponding conductivity reconstructions (right column): intact specimen (top row), the same specimen after major cracking (second row), middle sized crack (third row) and a very narrow crack (bottom row).*

### 5.3.2 Crack identification with adaptive meshing approach

In this section, a novel computational approach developed in publication **IV** for localizing cracks in solid materials is reviewed. The basic idea is to modify the conventional forward problem of ERT such that the geometrical model for the crack is explicitly written in the forward problem. This is achieved by formulating the crack estimation problem as a boundary estimation problem, in which the Neumann zero boundary condition is imposed on the crack boundary. That is, the cracks are assumed to be perfectly insulating. The similar crack identification problems (with perfectly insulating or conducting cracks) were first studied by Friedman and Vogelius in [116]. This work was further developed and analyzed in [117, 158–160]. The crack identification based on the aforementioned principles has also excited numerous other studies, see e.g. [161–172]. A more complete review on crack identification problems can be found in [173]. These earlier studies have clearly demostrated the feasibility of crack identification methods based on ERT, however, there still exist a few challenges to be considered. For example, the conductivity distribution is often assumed to be either known *a priori* or constant, or both. This is a serious limitation when imaging heterogeneous materials such as concrete.

In this thesis, we further develop the crack identification approach for more practical NDT applications. We aim to estimate the crack depth and orientation simultaneously with inhomogeneous background conductivity in 3D planar geometries where only one surface is available for ERT measurements. The crack model is obtained through some suitable low-order parametrization and these model parameters are then estimated together with the background conductivity. Because the geometry of the computational domain depends on the crack model, the finite element mesh used to solve the forward problem changes every time the model parameters of the crack are changed. This problem is tackled with a FE-meshing scheme that adaptively adjusts to the changes of the crack shape and location. This approach was presented for rebar localization first in [124] and **III**. In **IV** the method was tailored for crack detection. The approach is partly related to shape estimation problems that have been previously considered in inverse problems, see e.g. [174–177]. Here, the proposed approach is evaluated with simulated and real data.

## Crack modeling and estimation

Let $\Omega_b \subset \mathbb{R}^d$, $d = 2, 3$, denote a bounded domain that represents a target that consists of two parts: the volume of the solid material $\Omega \subset \Omega_b$ and the volume(s) of the crack(s) $\Omega_c = \Omega_b \setminus \Omega$. Denote the boundaries of $\Omega_b$ and $\Omega_c$ by $\partial\Omega_b$ and $\partial\Omega_c$, respectively. The boundary of the solid material is $\partial\Omega = \partial\Omega_b^{'} \cup \partial\Omega_c^{'}$ where $\partial\Omega_b^{'} = \partial\Omega_b \setminus (\partial\Omega_b \cap \partial\Omega_c)$ and $\partial\Omega_c^{'} = \partial\Omega_c \setminus (\partial\Omega_b \cap \partial\Omega_c)$. Note that with these notations $\partial\Omega_b \cap \partial\Omega_c \neq \emptyset$ corresponds to a case of a surface-breaking crack. In ERT, the electrodes $e_\ell$, $\ell = 1, \ldots, N_{el}$ are related to the boundary $\partial\Omega_b^{'}$ of the target domain $\Omega$ such that the electrodes do not cover the crack opening in the case of surface breaking crack. In order to estimate the position of the crack based on ERT measurements, we write some (low order) parametric representation for the crack. Denote the parameters defining the crack by $\theta \in \mathbb{R}^L$; then, formally, $\Omega_c = \Omega_c(\theta)$, $\Omega = \Omega(\theta)$. An example of the target domain and the crack parametrization is shown in Figure 5.6.

The formalism given above leads to a modification of the boundary condition (4.4) of CEM (4.1) – (4.6), that is

$$\sigma(x)\frac{\partial u(x)}{\partial \bar{n}} = 0, \quad \begin{cases} x \in \partial\Omega_b^{'} \setminus \bigcup_{\ell=1}^{N_{el}} e_\ell \\ x \in \partial\Omega_c^{'}(\theta) \end{cases} \tag{5.1}$$

thus resulting an observation model

$$V = R(\sigma, z, \theta) + e, \qquad e \sim \mathcal{N}(e_*, \Gamma_e) \tag{5.2}$$

which is similar to (4.13) with the exception of crack parametrization $\theta$ that affects the boundary $\partial\Omega$. As a consequence, the shape of the computational domain $\Omega$ and the Neumann boundary $\partial\Omega_c^{'}$ in the finite element approximation for the CEM is linked to the parametrization $\theta$. As in Section 4.4, the measurement noise $e$ is modeled as additive Gaussian noise with mean $e_*$ and covariance $\Gamma_e$.

The boundary parameters $\theta$ of the crack are estimated simultaneously with the discretized background conductivity distribution $\sigma$ and the contact impedances $z$ by computing the MAP estimate as in Section 4.4:

$$\Phi_{\text{MAP}} = \arg\max_{\Phi} \pi(\Phi|V) = \arg\min_{\Phi} F(\Phi; V), \tag{5.3}$$

where $\Phi = (\sigma^T, z^T, \theta^T)^T$ is a stacked vector form of the unknowns. The functional $F(\Phi; V)$ to be minimized is

$$F(\Phi; V) = \|L_e(V - R(\Phi))\|^2 + \|L_\Phi(\Phi - \Phi_*)\|^2, \tag{5.4}$$

where $\Phi_* = (\sigma_*^T, z_*^T, \theta_*^T)^T$ is the mean of $\Phi$. In equation (5.4), $L_e$ and $L_\Phi$ are Cholesky factors of the inverses of the covariance matrices $\Gamma_e$ (noise) and $\Gamma_\Phi$ (unknowns), such that $L_e^T L_e = \Gamma_e^{-1}$ and $L_\Phi^T L_\Phi = \Gamma_\Phi^{-1}$.

The MAP-estimate (5.3) is obtained through Gauss-Newton (GN) algorithm equipped with a step-size line-search and positivity constraint for $\sigma$ and $z$. With this GN-method, the crack parametrization $\theta$ is estimated by adaptively regenerating the finite element mesh along the iterative process. The Gauss-Newton algorithm involves the computation of the Jacobian matrix $J_\Phi = (J_\sigma, J_z, J_\theta)$ of the forward mapping with respect to the unknowns. The differentiation with respect to conductivity $\sigma$ and contact impedances $z$ have been previously discussed in [137] and [143], respectively. In publication **IV**, the matrix block $J_\theta$ of the Jacobian was computed by numerical "brute force" technique called *perturbation method*, such that

$$J_{\theta_k}^i = \frac{\partial R(\sigma^i, z^i, \theta^i)}{\partial \theta_k^i} \approx \frac{R(\sigma^i, z^i, \theta_\Delta^i) - R(\sigma^i, z^i, \theta^i)}{\Delta\theta_k^i}, \tag{5.5}$$

where $\sigma^i$, $z^i$ and $\theta^i$ are the estimates corresponding to $i^{\text{th}}$ iteration step, $\Delta\theta_k^i$ is a small perturbation in $k^{\text{th}}$ component of $\theta^i$ and $\theta_\Delta^i$ is the perturbed parametrization vector with $k^{\text{th}}$ component updated as $\theta_{\Delta k}^i = \theta_k^i + \Delta\theta_k^i$.

Once the Jacobians are computed, the search direction of the current GN-iteration step can be solved and the estimates are updated. The finite element mesh is regenerated on the basis of every update to $\theta^i$. For more details on the adaptive meshing approach, refer to **IV**.

## Results

In **IV**, numerical and experimental tests were performed in order to evaluate the performance of the adaptive meshing approach for crack identification. In the following, the main findings of these tests are discussed.

A simulational studies were conducted to test the adaptive meshing approach for identifying cracks in materials with homogeneous and inhomogeneous background conductivity. The crack was modeled as a rectangular shaped cuboid in a three dimensional domain. The crack was parametrized by the center point $(x_1^c, x_2^c, x_3^c)$ on the top of the crack, the crack length $l_c$, the crack depth $d_c$ and the angle $\beta = \beta(\bar{b}, -\bar{n}_c)$ between the downwards pointing vector $\bar{b} = (0, 0, -1)$ and the negative of the outwards pointing, top surface normal $\bar{n}_c$ of the crack. Thus, the parametrization in vectorized form is $\theta = (x_1^c, x_2^c, x_3^c, l_c, d_c, \beta)^T \in \mathbb{R}^6$. The crack parametrization in beam geometry is shown in Figure 5.6.

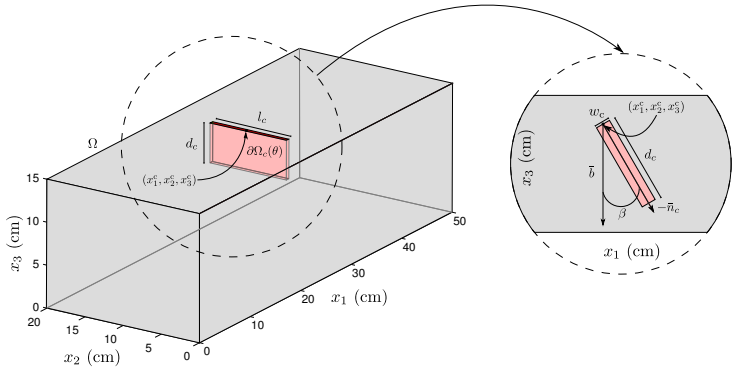


*Figure 5.6: The parametrization $\theta$ of a crack crack domain $\Omega_c(\theta)$ and its boundary $\partial\Omega_c(\theta)$ in target domain $\Omega$ (beam geometry).*

To simulate the measurements, the crack parameters were set as $\theta =$ (25 cm,10 cm,15 cm,10 cm,$d_c$ cm,$\beta^\circ)^T$, where parameters $d_c$ and $\beta$ varied depending on the case. As for the measurement noise, we added Gaussian random noise with standard deviation 0.05% of the difference between maximum and minimum value of the simulated voltages to the data. The selected noise level has been shown to represent well the noise level of a modern EIT system [114]. For comparison, the reconstructions based on the simulated data were also computed using the method described previously in Section 5.3.1. In the following, these reconstructions are referred as *standard reconstructions*. For more details, see publications **II** and **IV**.

The crack estimation was first tested with different crack cases in uniform background conductivity. It was found, that the adaptive meshing approach yields more accurate estimates for the crack depth and orientation than the standard method. Moreover, the adaptive meshing approach was found *robust* in that sense that it did not produce false crack estimate for an intact target. The results concerning the uniform background cases can be found in publication **IV**.

A more challenging test case was created by setting an inhomogeneous background conductivity distribution $\sigma = \sigma(x_3)$ defined in $\Omega = [0, 50] \times [0, 20] \times [0, 15] \setminus \Omega_c$, such that

$$\sigma(x) = \frac{0.09 \text{ mS/cm}}{15 \text{ cm}}(15 \text{ cm} - x_3) + 0.01 \text{ mS/cm}, \qquad x \in \Omega.$$

The crack depth and angle were $d_c = 5$ cm and $\beta = 0^\circ$, respectively. For

the conductivity, an anisotropic smoothness prior was used for both the standard method and for the adaptive meshing approach.

The results of the inhomogeneous case are shown in Figure 5.7 as 3D (left column) and cross-sectional representations (right column). The true conductivity distribution and the crack location are shown on the top row in Figure 5.7. The second row shows the reconstructed conductivity distribution corresponding to the standard method. On the third row, a result for the adaptive meshing approach with assumption of constant background conductivity is shown. The bottom row corresponds to the results of the adaptive meshing approach. In the standard reconstruction, the crack is at least faintly visible but its size (depth and length) is difficult to determine accurately from the reconstruction. The adaptive meshing approach fails to estimate the correct crack position and orientation when the background conductivity is forced to be constant. When the inhomogeneity of the background conductivity is taken into account, the crack estimate given by the adaptive meshing approach for the position and depth of the crack is good, $(x_1^c, x_2^c, x_3^c) \approx$ (24.7 cm, 9.9 cm, 14.9 cm) and $d_c \approx 5.5$ cm (see **IV**, Table I, Target 5). The estimated background conductivity given by the adaptive meshing approach has a strong resemblance with the true background conductivity. The standard method is clearly inferior in reconstructing the background conductivity.

The results for the experimental case are shown in Figure 5.8. The specimens are the same used in Section 5.3.1 and publication **II**. The left column in the figure shows schematic representations of two concrete slab specimens (dimensions 50 cm $\times$ 50 cm $\times$ 4 cm) with embedded plastic sheets of different depth-size. The corresponding reconstructions obtained with the adaptive meshing approach are shown on the right column. The top row in Figure 5.8 shows the specimen with plastic sheet of size 155 mm $\times$ 40 mm $\times$ 2 mm (i.e. the crack was 4 cm deep) and the reconstructed crack and background conductivity. On the bottom row, the case with 2.5 cm deep crack is shown. In both cases, the estimated crack boundaries are very similar to the synthetic cracks in the schematic pictures. In addition, the reconstructed conductivity distributions clearly show that the conductivity of concrete is nouniform. The estimated crack parameters are listed in **IV**, Table 2.

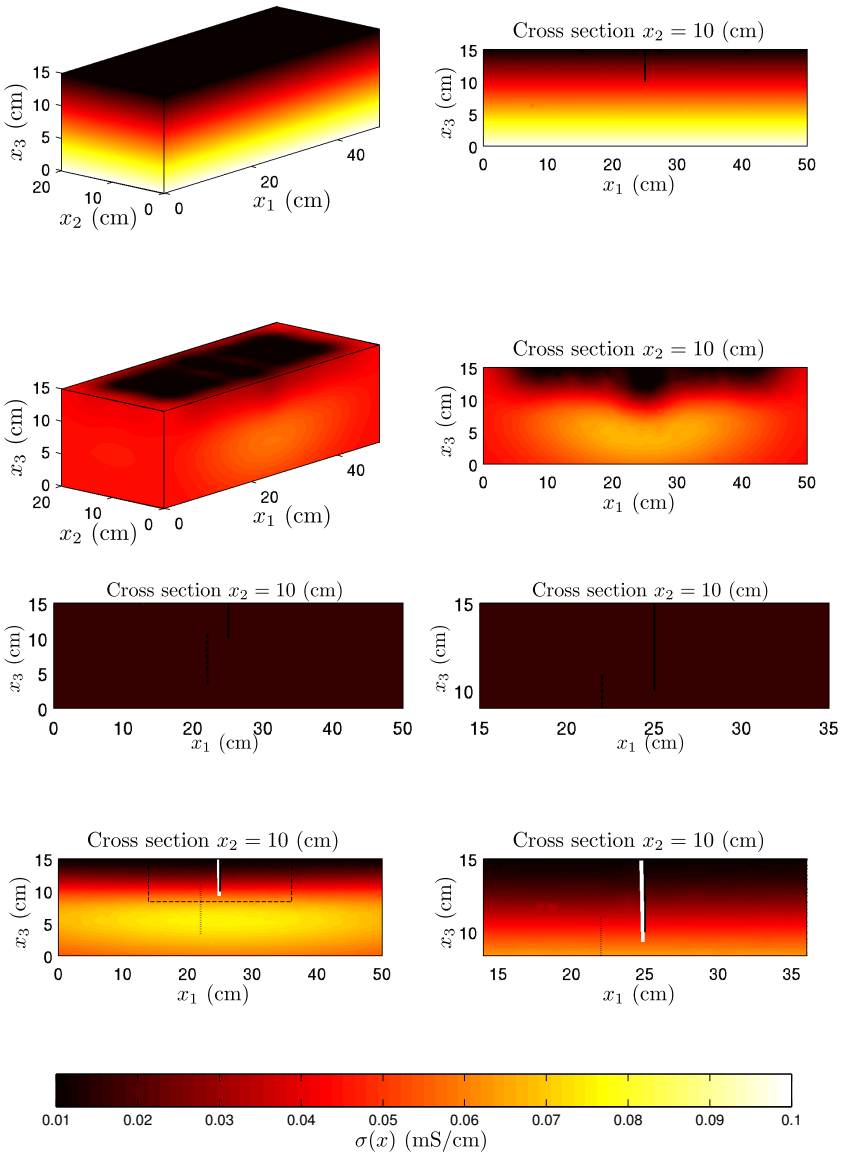


*Figure 5.7: Crack reconstructions from the simulation with inhomogeneous conductivity distribution. The true conductivity distribution is shown on top row. Second row: the reconstructions using the standard (anisotropic) smoothness prior. Thrid row: the results obtained using adaptive meshing algorithm with assumption of constant background. Bottom row) adaptive meshing approach with assumption of inhomogeneous background. The black line depicts the true crack and the white line is the estimated crack.*

### 5.3.3 Discussion

In **II**, plastic sheets were used for modeling cracks in the slab cases. This was because the locations and sizes of the synthetic cracks (plastic sheets) are easier to determine for validation of ERT reconstruction than those of real cracks. The reconstructions clearly reveal the areas with low conductivity and the sizes and shapes of the sheets are relatively well recovered (Figure 5.4). However, the widths of the poorly conductive areas were over-estimated. This was expectable since ERT is not very sensitive to the width of insulating crack. Moreover, smoothness prior was employed in a relatively coarse FE-meshes which causes additional "blurring" of the crack estimates. Because the aim in this experiment was mainly tracking the depths of the cracks, the effect of mesh refinement on the thickness estimates was not studied. In the delamination case, the dimensions of the plastic sheet were overestimated. This was for several reasons. First, in the case of slab geometry, the ERT measurements carry information mostly on the conductivity variations in the volume below the area covered by the electrode array. In this experiment, the dimensions of the laminar plastic were relatively large in comparison with the dimension of the electrode array. Thus, the measurements were not very sensitive to conductivities near the edges of the plate. Second, the ERT measurements are not sensitive to conductivities below the top surface of the plastic sheet because the insulating plastic parallel to the measurement surface blocks the current thus "cloaking" the volume underneath. As a result the uncertainty of the estimate is high at the edges and below the sheet (far from electrodes) and the estimates mostly rely on the implemented priors in those volumes. In this case, an anisotropic smoothness prior was used — a choice that favors high smoothness horizontally. For more thorough discussion, see **II**.

In the experiment with real cracks, the reconstructions of the first and second cases (the beam before cracking (intact) and after cracking (cracked), shown on top and second row in Figure 5.5) reveal the difference between the intact and the cracked state well. In addition, the estimated background conductivities for each case are quite homogeneous and close to each other; this is an appealing result since the same specimen was used for both cases. Note, that although this specimen was measured before and after cracking, the measurements acquired from the intact state were not used in reconstructing the conductivity distribution of the cracked state. Obtaining feasible reconstructions in both cases using exactly same reconstructions parameters indicates that the prior models used in the reconstructions were not too determinative. The reconstruc-

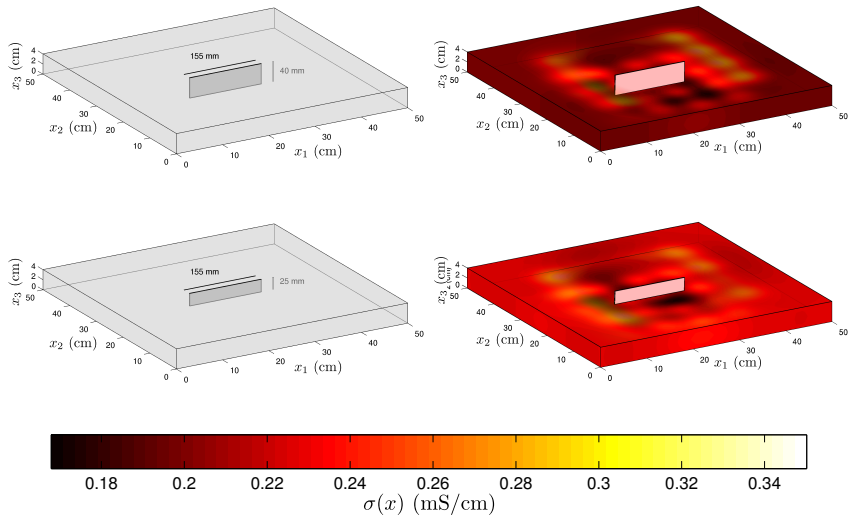


*Figure 5.8: Crack reconstructions from experimental data. On the left column schematic drawings of the specimens are shown and the corresponding reconstructions are on the right column. In the reconstructed images, both the crack (the light red area in the center) and the conductivity distribution are visualized.*

tion of the crack with crack opening of approximately 300 $\mu$m (third row in Figure 5.5) shows a region of low conductivity around the visually inspected crack. The conductivity under the region where the crack is visually observable is also lower than the background conductivity. This is most likely due to the occurrence of microcracking in this domain. The reconstruction for the crack with opening of 100 $\mu$m (bottom row in Figure 5.5) is not as good as in the previous case.

Based on the results in **IV**, it is clear that the crack estimates are more accurate when using the adaptive meshing approach than using the standard method. This is especially the case when the background conductivity is highly inhomogeneous (Figure 5.7). The results (Figure 5.7) show that it is difficult to deduce the crack depth from the standard reconstruction whereas the adaptive meshing approach gives good results.

In Figure 5.8, corresponding to experimental study with slabs, the reconstructed conductivity distributions reveal that the conductivity of concrete is clearly non-uniform: the conductivity of concrete varies due to different phases (cement paste, aggregate and air voids) and also due to moisture gradients and various local chemical properties of the cement paste. It should also be noted that some of the inhomogeneities may be

artefacts resulting from modeling and measurement errors. Especially, in this experiment the electrode contact impedances were observed to be unstable, i.e. the contact impedances varied during the set of measurements collected for one ERT-reconstruction.

## 5.4 LOCALIZATION OF REBARS

One of the fundamental reasons leading to decreased structural capacity of reinforced concrete is the corrosion of the steel reinforcement. The steel rebars are vulnerable to corrosion, for example, because of misplacement of the rebars during construction. Consequently, reliable testing methods are needed for assessing the condition and location of the rebars. Traditionally, electrical methods have been found suitable for such work (see section 3.3), however, most of the methods currently in use are based on relatively simplistic models of electromagnetism that are not capable to take full advantage what the electrical measurements can offer.

Furthermore, in previous works **I** and **II**, it was stated that rebars, being perfect conductors, have a high impact on electrical measurements. In order to succeed in estimating any concrete property on the basis of ERT measurements, the accurate modeling of the rebars is often a necessity. In **III**, a new approach for ERT was developed which allows more accurate modeling of the high conductivity of steel and the contact impedance between the reinforcing steels and the concrete. The rebar localization approach was tested with simulations.

When the target is not assumed to include internal metals, the electrodes $e_\ell$ in CEM (equations (4.2) – (4.4)) consist of measuring electrodes attached to the boundary of the target. This is the usual case in ERT imaging. Heikkinen et al. [123] proposed a novel approach in which known internal metallic structures are taken into account in ERT reconstruction. In the cited paper, the geometries of the internal metals were modeled, and they were considered as additional electrodes. That is, in this approach the total number of electrodes is $N_{\text{tot}} = N_{el} + N_D$ , where $N_{el}$ is the number of boundary electrodes and $N_D$ is the number of internal metals. In this section, the rebars are modeled as internal electrodes, whose positions and sizes are estimated. For this reason, a new parametrization variable is introduced, which includes rebar location parameters similarly to crack parametrization in section 5.3.2. In addition, this formalism allows current injection through the rebars, which can decrease the ill-posedness of the problem.

The discussion in this section based on publication **III**. The rebar localization method is based on the adaptive meshing scheme that was first studied in [124]. In **III**, the method was further developed for accounting multiple rebars and estimating their sizes. The theoretical part of **III** that considers the Fréchet derivative of the forward operator with respect to the location and shape of the rebars is omitted in this section. For details, see **III**.

### 5.4.1 Forward model and estimation

Let $\Omega \subset \mathbb{R}^d$, $d = 2, 3$, be an open bounded object that is partially covered with electrodes $e_\ell \subset \partial\Omega$, $\ell = 1, \ldots, N_{el}$. All electrodes are used for both current injection and voltage measurement, and the corresponding electrode currents and potentials are denoted by $I_\ell \in \mathbb{R}$ and $U_\ell \in \mathbb{R}$, respectively. Furthermore, $\Omega$ is assumed to be contaminated by ideally conducting and open inclusions $D_l$, $l = 1, \ldots, N_D$, for which $\overline{D}_l$ are mutually disjoint, have connected complements and lie within $\Omega$. The union of all the inclusions $D_l$ is denoted by $D$ and the corresponding inclusion potentials by $W_l \in \mathbb{R}$. In some cases, it is possible to inject currents through these inclusions and measure the corresponding potentials. Here, the inclusion currents are denoted by $J_l \in \mathbb{R}$ which may be zero if the inclusion $D_l$ is not available for measurements.

In this thesis, the contact impedances $z_\ell$, $\ell = 1, \ldots, N_{el}$ of the boundary electrodes and the contact impedances $\zeta_l$, $l = 1, \ldots, N_D$ of the embedded inclusions are assumed to be real valued and positive, i.e. $z_\ell$, $\zeta_l \in \mathbb{R}_+$. With this convention, the forward problem corresponding to the CEM (4.1) – (4.4) takes the form

$$\nabla \cdot \sigma(x) \nabla u(x) = 0, \qquad x \in \Omega \setminus \overline{D}, \tag{5.6}$$

$$\int_{e_\ell} \sigma(x) \frac{\partial u(x)}{\partial \bar{n}} \, dS = I_\ell, \qquad \ell = 1, \ldots, N_{el}, \tag{5.7}$$

$$\int_{\partial D_l} \sigma(x) \frac{\partial u(x)}{\partial \bar{n}} \, dS = J_l, \qquad l = 1, \ldots, N_D, \tag{5.8}$$

$$u(x) + z_\ell \sigma(x) \frac{\partial u(x)}{\partial \bar{n}} = U_\ell, \qquad x \in e_\ell, \ell = 1, \ldots, N_{el}, \tag{5.9}$$

$$u(x) + \zeta_l \sigma(x) \frac{\partial u(x)}{\partial \bar{n}} = W_l, \qquad x \in \partial D_l, l = 1, \ldots, N_D, \tag{5.10}$$

$$\sigma(x) \frac{\partial u(x)}{\partial \bar{n}} = 0, \qquad x \in \partial\Omega \setminus \bigcup_{\ell=1}^{N_{el}} e_\ell, \tag{5.11}$$

where the equations (5.8) and (5.10) define the inclusion currents and potentials, respectively. The total current vector is $\mathcal{I}^T = (I^T, J^T) \in \mathbb{R}^{N_{el}+N_D}$, where $I = (I_1, \ldots, I_{N_{el}})^T$ and $J = (J_1, \ldots, J_{N_D})^T$. Equivalently to (4.5), it is required that

$$\sum_{k=1}^{N_{el}+N_D} \mathcal{I}_k = 0,$$

and the reference level for the total potential vector $\mathcal{U}^T = (U, W)^T \in R^{N_{el}+N_D}$ can be fixed accordingly to equation (4.6).

The boundaries $\partial D_l$, $l = 1, \ldots, N_D$ of the inclusions are defined through the parametrization $\theta \in \mathbb{R}^n$. Thus the observation model is

$$V = R(\sigma, \bar{z}, \theta) + e, \qquad e \sim \mathcal{N}(e_*, \Gamma_e), \tag{5.12}$$

where $\bar{z}^T = (z^T, \zeta^T) \in \mathbb{R}^{N_{el}+N_D}$, $z = (z_1, \ldots, z_{N_{el}})^T$ and $\zeta = (\zeta_1, \ldots, \zeta_{N_D})^T$. As previously, the measurement noise $e$ is modeled as additive Gaussian noise with mean $e_* = 0$ and covariance $\Gamma_e$. The noise consisted of two components, such that the standard deviation of the first component was assumed to be 1% of the absolute noisy measurement voltage, and the standard deviation of the second component was assumed to be 0.1% of the absolute value of the difference between maximum and minimum noisy voltages.

Correspondingly to Section 5.3.2, the boundary parametrization $\theta$ of the inclusions (rebars) is estimated simultaneously with the discretized conductivity distribution $\sigma$ and the contact impedances $z$ by computing the MAP estimate $\Phi_{\text{MAP}} = \arg\min_\Phi F(\Phi; V)$ where $\Phi = (\sigma^T, \bar{z}^T, \theta^T)^T$ is a stacked vector form of the unknowns. The MAP estimate $\Phi_{\text{MAP}}$ is computed by finding a minimizer of the functional $F(\Phi; V)$ iteratively using the GN-method equipped with a step-size line search. On every GN-iteration and every update to the parametrization $\theta$ the rebars move and/or deform thus changing the computational mesh. The changes in the mesh are handled by employing the adaptive meshing approach similarly as in **IV** and Section 5.3.2. In this case, however, the Jacobian matrix $J_\Phi^i$ (corresponding to the $i^{\text{th}}$ iteration) of the forward mapping $\Phi^i \mapsto R(\Phi^i)$ with respect to the shape of the inclusion is computed (semi-) analytically using Corollary 3.3 in **III** instead of the equation (5.5) in the crack estimation case. With this approach, the computational time needed to compute the Jacobian matrix block $J_\theta^i$ can be decreased considerably. The rebar boundaries need to be "sufficiently smooth" in order to satisfy the assumptions of the approach. For details, see **III** and the Corollary 3.3 therein.

### 5.4.2 Results

A series of simulations were conducted to test the proposed method. In all test cases, $\Omega$ was a three-dimensional cylinder with radius 7.5 cm and height 3 cm. The considered rebars were smaller cylinders with central axes parallel to that of $\Omega$ and of the same height as $\Omega$. The background conductivity was chosen to represent typical conductivity of dry concrete found indoors (see Table 2.1), that is $\sigma = 5 \cdot 10^{-3}$ mS/cm. In the simulations, the aim was to estimate the locations of the rebars together with the value of the constant background conductivity $\sigma$. In some test cases, also the radii of the rebars were estimated. The contact impedances on the electrodes and inclusions were assumed to be known. In the following, the first and last simulational cases of publication **III** are considered. For the details of the full simulational study, see **III**.

In the first simulational case, one inaccessible rebar with known radius was located close to the boundary $\partial\Omega$. Here, the term "inaccessible" means that the rebar cannot be used for measurements and it is not possible to inject current through it. The task is to find the location of the rebar from boundary voltage measurements. The radius of the rebar was assumed to be known. The results are shown in Figure 5.9: the top left image illustrates the progress of the iterative algorithm for three initial guesses. The estimated boundary of the rebar is indicated by solid line and the central axis by '+'. The true boundary is drawn by dashed line. The "adaptation" of the finite element mesh to the rebar position estimate is illustrated in the five other images in Figure 5.9. The mesh images correspond to the "iteration path" drawn by a thick line in the top left image. In this simple case, the algorithm converges reliably and the reconstruction does not depend much on the initial guess.

In the last simulation of **III**, two test cases were studied to evaluate the method for estimating the locations and radii of two rebars inside the concrete body. The results are shown in Figure 5.10: The left column depicts the true targets with two rebars inside the concrete. The middle column illustrate the progress of the iterative algorithm without current injection through a rebar, and the right column shows the evolution of the iterative progress when current is injected through the rebar. In all tests, the same initial guess for the locations and radii of the rebars was used. In the first case shown on the top row of Figure 5.10, the convergence is a bit faster and the final reconstruction slightly better when current is injected through the rebars. For the geometry considered in the bottom row, the situation is more challenging. The accurate reconstruction in the bottom

right image of Figure 5.10 is obtained after only a couple of iterations while the one in the middle of the bottom row does not even coincide with the true target geometry. In this case, it is evident that the use of the rebars as internal electrodes improves the reconstructions significantly.

### 5.4.3 Discussion

The executed numerical tests with simulated noisy data demonstrate that the proposed method reconstructs the sizes and locations of rebars relatively well in most cases even if they are not used for current injection and potential measurements. However, the accuracy of the reconstructions and the rate of convergence is greatly increased if the rebars are used as internal electrodes. This is intuitive since driving currents through the rebar forces higher current densities in the interior of the investigated body, which should make the problem less illposed – especially, if the rebar lies deep inside the object. This effect was well observed in the last test case (see Figure 5.10, bottom row) where the smaller rebar is located at the center of the object in the "shadow" of the larger rebar near the object boundary. In this case the measurements carry very little information about the location of the smaller rebar, if current is not driven through the rebars.

The simultaneous estimation of rebar location and radius performs relatively well with noisy data. However, by considering higher noise levels, one would encounter situations where the estimates would be accurate only if the rebar was used for measurements. When simultaneously estimating the radius with the locations, the algorithm tends to shrink the size of the rebar before the correct location is found. Intuitively, this means that an estimate without a rebar gives a better fit than one with a rebar far away from the true inhomogeneity.

The estimate of the constant conductivity $\sigma$ was also reliable and the convergence relatively fast in all numerical cases (refer to Figure 4.3 in **III**). In practice, however, the conductivity of concrete is often inhomogeneous due to distribution of moisture, chlorides, etc. In order to make the described method useful from the practical point of view, the estimation scheme needs to be tested with inhomogeneous conductivity distributions. The modification of the method to estimation of inhomogeneous conductivity distributions is straightforward.

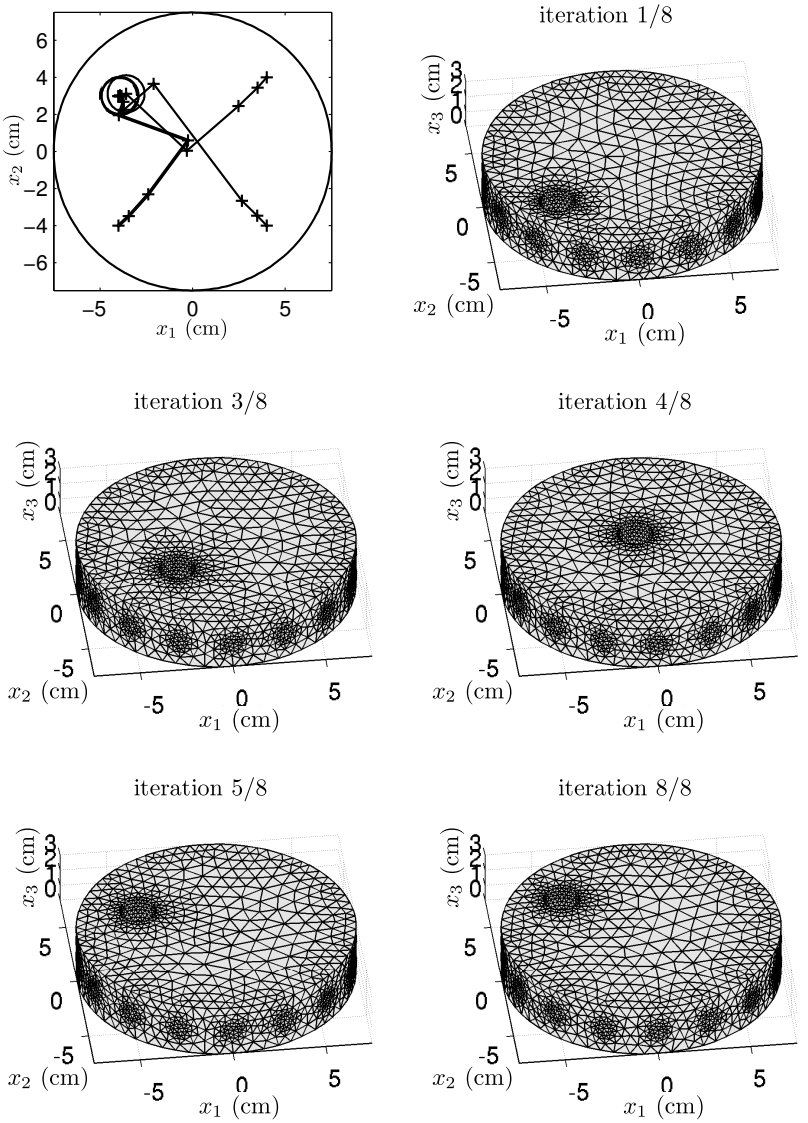


*Figure 5.9: Localization of a rebar positioned close to boundary. The evolution of the iterative progress for three initial guesses is shown on top left. The true position of the rebar is drawn by dashed line and the rebar centers are marked with '+'. The other images demonstrate the adaptation of the FE-mesh to the position estimate of the rebar. The mesh corresponds to the "iteration path" starting at coordinates (-4,-4) and drawn by thick line on top left.*

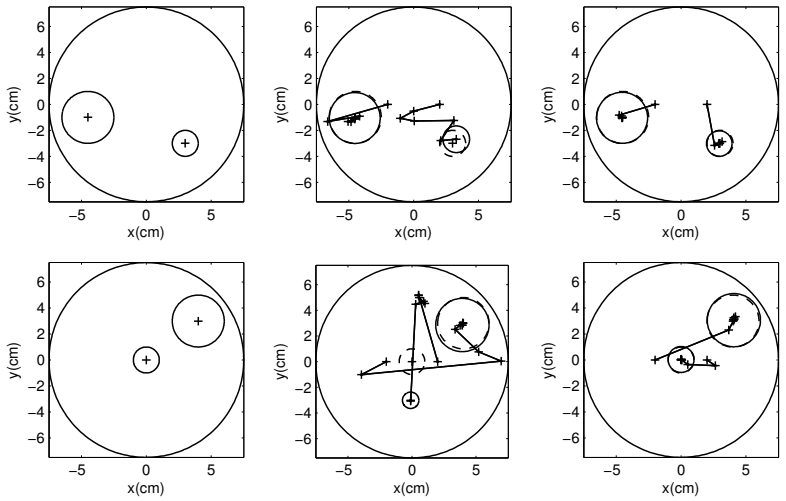


*Figure 5.10: Estimation of locations and radii for two rebars. Left column: the true targets. Middle column: the evolution of the iterative progress without current injection through rebars. Right column: the evolution with current injection through the rebars. The rebar boundaries corresponding to the final estimates are drawn by solid line and the true boundaries by dashed line. The rebar centers are marked with '+'.*

# 6 Summary and conclusions

The main emphasis of this thesis was to study the feasibility of ERT for non-destructive testing of concrete. The evaluation of the condition of concrete embodies various important factors. In this thesis, the imaging of internal conductivity distribution of concrete, identification of cracks and localization of reinforcing bars (i.e. rebars) were addressed. In order to succeed in the aforementioned tasks, novel computational schemes were developed for ERT and combined with state-of-the-art statistical inversion methods.

The research of ERT for NDT of concrete has been low in civil engineering community. The previous studies have reported the technique promising but not yet ready for practical applications [37–39, 109, 115]. The potential applications of ERT in the construction industry include detection of the thickness of the concrete cover on top of reinforcement bars and estimation of crack depths and moisture distributions.

In Publication **I**, the feasibility of ERT for detection of different inclusions in concrete was studied. This is the first paper in which ERT was applied successfully for imaging of concrete without utilizing reference data in the reconstructions. Concrete specimens cast with a polyuretane block, steel bars and plastic sheets were measured using ERT. The results indicate that different types of inclusions can be detected and localized using this method. The experiments were carried out using young samples that were relatively conductive. However, the ERT imaging scheme is not limited to conductive targets only: ERT has been successfully applied to various geophysical problems in which the targets are highly resistive; see for example [178–180]. In this series of experiments, all the samples were short cylinders and measurements were acquired around the target. In practice, most of the inspected targets share a beam or slab geometry and the measurements cannot be always acquired around the target. Such geometries were considered in the publications **II** and **IV**.

In Publication **II**, the feasibility of using ERT to localize and characterize cracks in concrete was tested. In this series of experimental and numerical tests, concrete slabs and beams were used, and the measurements were acquired from one surface only. In the first part of this study, slab specimens with plastic sheets were measured. The plastic sheets were used for modeling the cracks to reliably verify the locations of nonconductive regions. Sheets perpendicular to and parallel with the concrete

surface were considered. The results indicate that both types of inhomogeneities can be detected using ERT. Furthermore, the dimensions of the plastic sheets perpendicular to the concrete surface were estimated quite reliably, suggesting that the detection of crack depths using ERT may be possible. In the selected geometry, the depth resolution was on the order of a few millimeters. The estimated dimensions of the plastic sheet parallel to surface were not that accurate; this was the result of using a relatively small electrode array in comparison with the size of the sheet. In practice, however, the dimensions of large laminar cracks could be traced by separate ERT measurements using different array positions on the concrete surface.

In **II**, the applicability of using ERT to localize and characterize cracks was also tested using beam specimens with real cracks. These experiments verify that cracks in concrete can be detected using ERT. The experiments conducted on the beams support the results obtained in the previous experiments with slabs: ERT is capable of distinguishing between cracks of different depths. Further, this experiment gives an approximate estimate of the sensitivity of the method: it can be concluded that at least 300 $\mu$m wide cracks can be clearly detected. Even a 100 $\mu$m wide crack was detected, although the resolution was not as good as with larger crack widths. The results suggest that ERT could be potential tool for determining the crack widths. However, before applying the method in practice, the reliability of the modality for characterizing crack widths should be studied with large numbers of specimens. Such a study should include comparison of the ERT reconstructions with data provided by an alternative modality. In this study, the estimates of the real cracks were verified only by a qualitative visual inspection. The experiments reported herein were carried out using samples that were moist and therefore had a high conductivity.

In Publication **III**, a novel computational method was developed for estimating the locations and radii of rebars (inclusions) inside a body of concrete with constant but unknown background conductivity. One of the main aims was to develop a model for internal metals that have a high impact on electrical measurements. Since the internal metals act as electrodes, the traditional models based on continuous representation of the conductivity distribution are flawed. In this work, the embedded rebars were considered as internal electrodes whose shape and locations are unknown, but can be estimated on the basis of boundary voltage measurements. A special characteristic of this measurement setting is that in certain cases it is possible to use the rebars as electrodes for driv-

ing currents and measuring the corresponding "inclusion potentials" even though the locations of the rebars are not accurately known. For example, some bridge structures contain an additional contact steel that is in direct electrical contact with the embedded rebar mesh. The currents can be driven to the rebars through this contact steel.

As the unknown internal electrodes were part of the computational geometry, the conventional approaches for ERT could not be used. This problem was sorted out by employing an adaptive meshing scheme that iteratively adapts to the changes of the computational geometry. The method was tested in dimension three with simulated noisy data. The results show that the approach can be used for localizing rebars that are either accessible or inaccessible for measurements and/or current injections. However, the reconstructions become notably more accurate and the convergence of the algorithm significantly faster if current is injected through the rebars. In **III**, the background conductivity was assumed homogeneous in all simulations. The extension of the method to consider inhomogeneous conductivity distributions is, however, straightforward.

In **IV**, numerical and experimental tests were conducted in order to evaluate the adaptive meshing scheme for crack detection. The key idea was to model the crack detection problem as a boundary estimation problem, where Neumann zero boundary condition was imposed on the crack boundary. The boundary estimation was carried out by employing the adaptive meshing approach. The results show that the adaptive meshing approach can distinguish different crack sizes in cases of homogeneous and inhomogeneous background conductivities. In the case of inhomogeneous background, the method performs significantly better in crack detection than the conventional approach, especially, when the contrast between the lowest and the highest value of conductivity is high. The standard method performs relatively well in imaging of the cracks in low contrast inhomogeneous backgrounds, but poorly in reconstructing the background conductivity distribution. Although the employed crack model was relatively simple, the adaptive meshing approach is capable for more complex boundary representations. In fact, one of the advantages of the proposed approach is the freedom of choice for the parametrization.

In conclusions, this study has shown promise for ERT to become a potential tool for NDT of concrete. The modality has been shown to be applicable in estimating the location and size of cracks, localizing rebars and simultaneously reconstructing the (inhomogeneous) background conductivity of concrete. The 3D tomographic images reconstructed from an ERT measurement are easy to interpret and provide information that is

either impossible or hard to obtain when using other electrical methods. Furthermore, ERT may have potential in detection of crack widths, rebar corrosion and moisture and chloride distributions. Hence, by combining ERT with other NDT modalities, a more thorough look into the condition of concrete structures could be attained.

The biggest challenge in the ERT measurements of concrete arises from the contact problems between the electrodes and the concrete surface. The wet electrodes can provide a good contact to concrete but the contact is not stable with respect to time as the electrolyte of the electrodes is absorbed by the conrete specimen. Moreover, excessive absorbtion of the electrolyte can create contact paths between neighboring electrodes. The absorbtion problems are mostly avoided by using gel electrodes, however, the gel electrodes may have a slightly worse contact than that of wet electrodes, especially, with very dry concrete. In crack detection, small cracks with crack widths less than 100 $\mu$m cannot be reliably detected because after this limit the change in the electrical conductivity is no longer detectable. Another limitation of the method is its poor spatial resolution, especially, if compared to ultrasonic and radar methods. However, ERT is very sensitive to conductivity changes. Also an advantage is that the modality provides 3D reconstructions of the spatial conductivity distribution of concrete and makes it possible to take model uncertainties into account. With currently available electrical modalities this is not achievable. Furthermore, the prior models in ERT can be developed to meet the application specific needs.

In this thesis, pioneering work to study the feasibility of ERT in NDT of concrete was performed. The proposed method was studied with laboratory experiments and no field test were undertaken. Also, no quantitative comparison to other NDT methods was yet performed. In future, it is important to consider these two aspects in order to ERT to become a potential tool in NDT of concrete.

# *Bibliography*


[1] P. Mehta and P. Monteiro, *Concrete: microstructure, properties, and materials* (McGraw-Hill, 2006).

[2] E. Sullivan, D. Czechowski, D. Zwicke, M. Howard, and K. Arneson, *The U.S. Monitor*, Vol. 19, (Portland Cement Association, 2009).

[3] M. García-Alonso, M. Escudero, J. Miranda, M. Vega, F. Capilla, M. Correia, M. Salta, A. Bennani, and J. González, "Corrosion behaviour of new stainless steels reinforcing bars embedded in concrete," *Cement and concrete research* **37,** 1463–1471 (2007).

[4] J. Bungey and S. Millard, *Testing of concrete in structures*, 3 ed. (Chapman & Hall, 1996).

[5] J. Lataste, C. Sirieix, D. Breysse, and M. Frappa, "Electrical resistivity measurement applied to cracking assessment on reinforced concrete structures in civil engineering," *NDT & E International* **36,** 383–394 (2003).

[6] A. Peled, J. Torrents, T. Mason, S. Shah, and E. Garboczi, "Electrical impedance spectra to monitor damage during tensile loading of cement composites," *ACI Materials Journal* **98,** 313–322 (2001).

[7] T. Mason, M. Campo, A. Hixson, and L. Woo, "Impedance spectroscopy of fiber-reinforced cement composites," *Cement and Concrete Composites* **24,** 457–465 (2002).

[8] N. Ozyurt, L. Woo, T. Mason, and S. Shah, "Monitoring fiber dispersion in fiber-reinforced cementitious materials: comparison of AC-impedance spectroscopy and image analysis," *ACI materials journal* **103** (2006).

[9] L. Woo, N. Kidner, S. Wansom, and T. Mason, "Combined time domain reflectometry and AC-impedance spectroscopy of fiber-reinforced fresh-cement composites," *Cement and Concrete Research* **37,** 89–95 (2007).

[10] N. Ozyurt, T. Mason, and S. Shah, "Non-destructive monitoring of fiber orientation using AC-IS: An industrial-scale application," *Cement and concrete research* **36,** 1653–1660 (2006).

[11] P. Monteiro, F. Morrison, and W. Frangos, "Non-Destructive Measurement of Corrosion State of Reinforcing Steel in Concrete," *ACI Materials Journal* **95** (1998).

[12] J. Zhang, P. Monteiro, and H. Morrison, "Noninvasive Surface Measurement of Corrosion Impedance of Reinforcing Bar in Concrete — Part 1: Experimental Results," *ACI Materials Journal* **98** (2001).

[13] J. Zhang, P. Monteiro, and H. Morrison, "Noninvasive Surface Measurement of Corrosion Impedance of Reinforcing Bar in Concrete — Part 2: Forward Modeling," *ACI Materials Journal* **99** (2002).

[14] J. Zhang, P. Monteiro, H. Morrison, and M. Mancio, "Noninvasive Surface Measurement of Corrosion Impedance of Reinforcing Bar in Concrete — Part 3: Effect of Geometry and Material Properties," *ACI Materials Journal* **101** (2004).

[15] W. McCarter and S. Garvin, "Dependence of electrical impedance of cement-based materials on their moisture condition," *Journal of Physics D: Applied Physics* **22,** 1773 (1989).

[16] F. Hunkeler, "Monitoring of repaired reinforced concrete structures by means of resistivity measurements," *Materials Science Forum* **247,** 93–106 (1997).

[17] W. McCarter and H. Ezirim, "AC impedance profiling within cover zone concrete: influence of water and ionic ingress," *Advances in cement research* **10,** 57–66 (1998).

[18] J. Loche, A. Ammar, and P. Dumargue, "Influence of the migration of chloride ions on the electrochemical impedance spectroscopy of mortar paste," *Cement and concrete research* **35,** 1797–1803 (2005).

[19] G. Saulnier, R. Blue, J. Newell, D. Isaacson, and P. Edic, "Electrical impedance tomography," *Signal Processing Magazine, IEEE* **18,** 31–43 (2001).

[20] L. Borcea, "Electrical impedance tomography," *Inverse Problems* **18,** R99–R136 (2002).

[21] M. Cheney, D. Isaacson, and J. Newell, "Electrical impedance tomography," *SIAM review* **41,** 85–101 (1999).

[22] J. Kaipio, V. Kolehmainen, E. Somersalo, and M. Vauhkonen, "Statistical inversion and Monte Carlo sampling methods in EIT," *Inverse problems* **16,** 1487–1522 (2000).

[23] F. Dickin and M. Wang, "Electrical resistance tomography for process applications," *Measurement Science and Technology* **7,** 247 (1996).

[24] O. C. Jones, J. T. Lin, , and L. Ovacik, "Investigation of electrical impedance imaging relative to two-phase, gas-liquid flows," *Chem. Eng. Comm.* **118,** 299–325 (1992).

[25] L. M. Heikkinen, J. Kourunen, T. Savolainen, P. J. Vauhkonen, J. P. Kaipio, and M. Vauhkonen, "Real time three-dimensional electrical impedance tomography applied in multiphase flow imaging," *Meas. Sci. Technol.* **17,** 2083 (2006).

[26] R. Williams and M. Beck, *Process tomography: principles, techniques, and applications* (Butterworth-Heinemann, 1995).

[27] J. Mueller, D. Isaacson, and J. Newell, "A reconstruction algorithm for electrical impedance tomography data collected on rectangular electrode arrays.," *IEEE transactions on bio-medical engineering* **46,** 1379 (1999).

[28] K. Osterman, T. Kerner, D. Williams, A. Hartov, S. Poplack, and K. Paulsen, "Multifrequency electrical impedance imaging: preliminary in vivo experience in breast," *Physiological Measurement* **21,** 99–109 (2000).

[29] B. Brown, D. Barber, and A. Seagar, "Applied potential tomography: possible clinical applications," *Clinical Physics and Physiological Measurement* **6,** 109–121 (1985).

[30] P. Kunst, A. Noordegraaf, O. Hoekstra, P. Postmus, and P. De Vries, "Ventilation and perfusion imaging by electrical impedance tomography: a comparison with radionuclide scanning," *Physiological Measurement* **19,** 481–490 (1998).

[31] I. Frerichs, G. Hahn, and G. Hellige, "Thoracic electrical impedance tomographic measurements during volume controlled ventilation-effects of tidal volume and positive end-expiratory pressure," *IEEE Trans. Med. Imaging* **18,** 764–773 (1999).

[32] L. Bentley and M. Gharibi, "Two-and three-dimensional electrical resistivity imaging at a heterogeneous remediation site," *Geophysics* **69,** 674–680 (2004).

[33] P. Church, J. McFee, S. Gagnon, and P. Wort, "Electrical impedance tomographic imaging of buried landmines," *IEEE Transactions on Geoscience and Remote Sensing* **44,** 2407–2420 (2006).

[34] P. Soupios, I. Papadopoulos, M. Kouli, I. Georgaki, F. Vallianatos, and E. Kokkinou, "Investigation of waste disposal areas using electrical methods: a case study from Chania, Crete, Greece," *Environmental Geology* **51,** 1249–1261 (2007).

[35] T. Hou, K. Loh, and J. Lynch, "Spatial conductivity mapping of carbon nanotube composite thin films by electrical impedance tomography for sensing applications," *Nanotechnology* **18,** 315501 (2007).

[36] W. Daily, A. Ramirez, A. Binley, and S. Henry-Poulter, "Electrical resistance tomography of concrete structures," in *ECAPT94: 3rd European concerted action meeting on process tomography, March 24–27* (1994), p. 7.

[37] M. Buettner, A. Ramirez, and W. Daily, "Electrical Resistance Tomography for Imaging Concrete Structures," in *Structural Materials Technology and NDT Conference* (1995), p. 8.

[38] M. Buettner, A. Ramirez, and W. Daily, "Electrical Resistance Tomography for Imaging the Spatial Distribution of Moisture in Pavement Sections," in *Structural Materials Technology and NDT Conference* (1995), p. 8.

[39] T. Hou and J. Lynch, "Electrical impedance tomographic methods for sensing strain fields and crack damage in cementitious structures," *Journal of Intelligent Material Systems and Structures* **20,** 1363 (2009).

[40] A. Tarantola, *Inverse problem theory and methods for model parameter estimation* (Society for Industrial Mathematics, 2005).

[41] J. Kaipio and E. Somersalo, *Statistical and computational inverse problems* (Springer Science+ Business Media, Inc., 2005).

[42] S. Diamond, "The microstructure of cement paste and concrete–a visual primer," *Cement and Concrete Composites* **26,** 919–933 (2004).

[43] N. Martys and C. Ferraris, "Capillary transport in mortars and concrete," *Cement and Concrete Research* **27,** 747–760 (1997).

[44] D. Bentz, J. Hwang, C. Hagwood, E. Garboczi, K. Snyder, N. Buenfeld, and K. Scrivener, "Interfacial zone percolation in concrete: Effects of interfacial zone thickness and aggregate shape," *Material Research Society Symposium Proceedings* **370,** 437–442 (1995).

[45] R. Feldman and P. Sereda, "A new model for hydrated Portland cement and its practical implications," *Engineering Journal* **53,** 53–59 (1970).

[46] W. McCarter, M. Forde, and H. Whittington, "Resistivity characteristics of concrete," *Institution of Civil Engineers Proceedings pt. 2* **71,** 107–17 (1981).

[47] R. Polder, "Test methods for on site measurement of resistivity of concrete–a RILEM TC-154 technical recommendation," *Construction and building materials* **15,** 125–131 (2001).

[48] H. Whittington, J. McCarter, and M. Forde, "Conduction of electricity through concrete," *Magazine of Concrete Research* **33,** 48–60 (1981).

[49] G. Song, "Equivalent circuit model for AC electrochemical impedance spectroscopy of concrete," *Cement and concrete research* **30,** 1723–1730 (2000).

[50] W. McCarter, S. Garvin, and N. Bouzid, "Impedance measurements on cement paste," *Journal of Materials Science Letters* **7,** 1056–1057 (1988).

[51] W. McCarter and R. Brousseau, "The AC response of hardened cement paste," *Cement and Concrete Research* **20,** 891–900 (1990).

[52] W. McCarter, "A parametric study of the impedance characteristics of cement-aggregate systems during early hydration," *Cement and Concrete Research* **24,** 1097–1110 (1994).

[53] K. Brantervik and G. Niklasson, "Circuit models for cement based materials obtained from impedance spectroscopy," *Cement and concrete research* **21,** 496–508 (1991).

[54] W. McCarter, T. Chrisp, and H. Ezirim, "Discretized conductivity measurements to study wetting and drying of cover zone concrete," *Advances in cement research* **10,** 195–202 (1998).

[55] W. McCarter, "The ac impedance response of concrete during early hydration," *Journal of materials science* **31,** 6285–6292 (1996).

[56] L. Bell, T. Khan, K. Rear, R. Bohan, P. Krauss, R. Rivera-Villarreal, D. Burg, C. Lobo, J. Rose, D. Elliott, et al., "Reinforcement for Concrete — Materials and Applications," *ACI Education Bulletin E2-00* (2006).

[57] T. MacGinley and B. Choo, *Reinforced concrete: design theory and examples* (Taylor & Francis, 1990).

[58] P. Basheer, S. Chidiact, and A. Long, "Predictive models for deterioration of concrete structures," *Construction and Building Materials* **10,** 27–37 (1996).

[59] M. Abou-Zeid, D. Fowler, E. Nawy, J. Allen, G. Halvorsen, R. Poston, J. Barlow, W. Hansen, R. Rhoads, M. Brander, et al., "Control of Cracking in Concrete Structures," *ACI report 224R-01* 1–46 (2001).

[60] S. Yoon, K. Wang, W. Weiss, and S. Shah, "Interaction between loading, corrosion, and serviceability of reinforced concrete," *ACI materials journal* **97,** 637–644 (2000).

[61] D. McCann and M. Forde, "Review of NDT methods in the assessment of concrete and masonry structures," *NDT & E International* **34,** 71–84 (2001).

[62] O. Buyukozturk, "Imaging of concrete structures," *NDT and E International* **31,** 233–243 (1998).

[63] H. Wiggenhauser, "Advanced NDT methods for the assessment of concrete structures," in *Concrete Repair, Rehabilitation and Retrofitting: 2nd International Conference on Concrete Repair, Rehabilitation and Retrofitting, ICCRRR-2, 24-26 November 2008, Cape Town, South Africa* (CRC, 2008), pp. 19–31.

[64] C. Sirieix, J. Lataste, D. Breysse, S. Naar, and X. Dérobert, "Comparison of nondestructive testing: Infrared thermography, electrical resisitivity and capacity methods for assessing a reinforced concrete structure," *Journal of Building Appraisal* **3,** 77–88 (2007).

[65] C. Maierhofer, H. Reinhard, and G. Dobmann, *Non-destructive evaluation of reinforced concrete structures. Volume 2: Non-destructive testing methods* (Woodhead Publishing Ltd, 2010).

[66] D. Breysse, *Non-destructive Assessment of Concrete Structures: Reliability and Limits of Single and Combined Techniques: State-of-the-art Report of the RILEM Technical Committee 207-INR*, Vol. 1, (Springer, 2012).

[67] "Non-destructive testing," *Cement and Concrete Composites, Special issue* **28,** 297–414 (2006).

[68] M. Schickert, "Progress in ultrasonic imaging of concrete," *Materials and Structures* **38,** 807–815 (2005).

[69] M. Krause, M. Bärmann, R. Frielinghaus, F. Kretzschmar, O. Kroggel, K. Langenberg, C. Maierhofer, W. Müller, J. Neisecke, M. Schickert, et al., "Comparison of pulse-echo methods for testing concrete," *NDT & E International* **30,** 195–204 (1997).

[70] J. Krieger, M. Krause, and H. Wiggenhauser, "Tests and assessments of NDT methods for concrete bridges," in *Proceedings of SPIE*, Vol. 3400 (1998), p. 258.

[71] Y. Sakata and M. Ohtsu, "Crack evaluation in concrete members based on ultrasonic spectroscopy," *ACI materials journal* **92** (1995).

[72] M. Schickert, "Ultrasonic NDE of concrete," in *Ultrasonics Symposium, 2002. Proceedings. 2002 IEEE*, Vol. 1 (IEEE, 2003), pp. 739–748.

[73] M. Schickert, "Towards SAFT-Imaging in ultrasonic inspection of concrete," in *International Symposium Non Destructive Testing in Civil Engineering (NDT-CE)* (1995), pp. 411–418.

[74] M. Schickert, M. Krause, and W. Müller, "Ultrasonic imaging of concrete elements using reconstruction by synthetic aperture focusing technique," *Journal of materials in civil engineering* **15,** 235 (2003).

[75] V. Schmitz, M. Kröning, and K. Langenberg, "Quantitative NDT by 3D image reconstruction," *Acoustical Imaging* **22,** 735–44 (1996).

[76] K. Mayer, K. Langenberg, M. Krause, C. Maierhofer, B. Milmann, and C. Kohl, "Characterization of ultrasonic and radar reflector types in concrete by phase evaluation of the signal and the reconstructed image," in *Proceedings of the ECNDT 9th European Conference on NDT* (2006).

[77] M. Krause, F. Mielentz, B. Milmann, D. Streicher, and W. Müller, "Ultrasonic imaging of concrete elements: State of the art using 2D synthetic aperture," in *International Symposium of Nondestructive Testing in Civil Engineering (NDT-CE) in Berlin, Germany, September* (2003), pp. 16–19.

[78] Germann Instruments A/S, "Catalog NDT 2010," (2010).

[79] M. Sansalone, N. Carino, and C. for Building Technology. Structures Division, *Impact-echo: a method for flaw detection in concrete using transient stress waves* (US Dept. of Commerce, National Bureau of Standards, Center for Building Technology, Structures Division, 1986).

[80] M. Sansalone and N. Carino, "Detecting delaminations in concrete slabs with and without overlays using the impact-echo method," *ACI Materials Journal* **86,** 175–184 (1989).

[81] M. Ohtsu, "The history and development of acoustic emission in concrete engineering," *Magazine of Concrete Research* **48,** 321–330 (1996).

[82] M. Ohtsu, "Basics of acoustic emission and applications to concrete engineering," *Materials science research international* **4,** 131–140 (1998).

[83] D. Yoon, W. Weiss, and S. Shah, "Assessing damage in corroded reinforced concrete using acoustic emission," *Journal of engineering mechanics* **126,** 273–283 (2000).

[84] A. Nielsen, "Gamma-ray-attenuation used for measuring the moisture content and homogeneity of porous concrete," *Building Science* **7,** 257–263 (1972).

[85] W. Najjar, H. Aderhold, and K. Hover, "The application of neutron radiography to the study of microcracking in concrete," *Cement, Concrete and Aggregates* **8** (1986).

[86] R. Pugliesi and M. Andrade, "Study of cracking in concrete by neutron radiography," *Applied Radiation and Isotopes* **48,** 339–344 (1997).

[87] F. De Beer, J. Le Roux, and E. Kearsley, "Testing the durability of concrete with neutron radiography," *Nuclear Instruments and Methods in Physics Research Section A: Accelerators, Spectrometers, Detectors and Associated Equipment* **542,** 226–231 (2005).

[88] H. Martz, G. Roberson, M. Skeate, D. Schneberk, and S. Azevedo, "Computerized tomography studies of concrete samples," *Nuclear Instruments and Methods in Physics Research Section B: Beam Interactions with Materials and Atoms* **58,** 216–226 (1991).

[89] H. Martz, D. Scheberk, G. Roberson, and P. Monteiro, "Computerized tomography analysis of reinforced concrete," *ACI Materials Journal* **90** (1993).

[90] E. Hussein and T. Whynot, "A Compton scattering method for inspecting concrete structures," *Nuclear Instruments and Methods in Physics Research Section A: Accelerators, Spectrometers, Detectors and Associated Equipment* **283,** 100–106 (1989).

[91] M. Clark, D. McCann, and M. Forde, "Application of infrared thermography to the non-destructive testing of concrete and masonry bridges," *NDT & E International* **36,** 265–275 (2003).

[92] C. Maierhofer, R. Arndt, M. Röllig, C. Rieck, A. Walther, H. Scheel, and B. Hillemeier, "Application of impulse-thermography for non-destructive assessment of concrete structures," *Cement and Concrete Composites* **28,** 393–401 (2006).

[93] J. Alldred, J. Chua, and D. Chamberlain, "Determination of reinforcing bar diameter and cover by analysing traverse profiles from a cover meter," *Non-Destructive Testing in Civil Engineering(NDT-CE).* **1,** 721–728 (1995).

[94] J. Bungey, "Sub-surface radar testing of concrete: a review," *Construction and Building Materials* **18,** 1–8 (2004).

[95] S. Hubbard, J. Zhang, P. Monteiro, J. Peterson, and Y. Rubin, "Experimental detection of reinforcing bar corrosion using nondestructive geophysical techniques," *ACI Materials Journal* **100** (2003).

[96] S. Millard and J. Harrison, "Measurement of the electrical resistivity of reinforced concrete structures for the assessment of corrosion risk," *Brit. J. Nondestructive Testing* **31,** 617–621 (1989).

[97] S. Millard, M. Ghassemi, J. Bungey, and M. Jafar, "Assessing the electrical resistivity of concrete structures for corrosion durability studies," *Corrosion of reinforcement in concrete* 303–313 (1990).

[98] M. Saleem, M. Shameem, S. Hussain, and M. Maslehuddin, "Effect of moisture, chloride and sulphate contamination on the electrical resistivity of Portland cement concrete," *Construction and Building Materials* **10,** 209–214 (1996).

[99] J. Lataste, M. Behloul, and D. Breysse, "Characterisation of fibres distribution in a steel fibre reinforced concrete with electrical resistivity measurements," *NDT & E International* **41,** 638–647 (2008).

[100] W. McCarter, T. Chrisp, A. Butler, and P. Basheer, "Near-surface sensors for condition monitoring of cover-zone concrete," *Construction and Building Materials* **15,** 115–124 (2001).

[101] M. Mancio, M. Eng, J. Zhang, and P. Monteiro, "Nondestructive Surface Measurement of Corrosion of Reinforcing Steel in Concrete," *Canadian Civil Engineer* **21,** 12–14 (2004).

[102] R. Henderson and J. Webster, "An impedance camera for spatially specific measurements of the thorax," *IEEE Transactions on Biomedical Engineering* 250–254 (1978).

[103] R. Lytle and K. Dines, "Impedance camera: a system for determining the spatial variation of electrical conductivity," (1978), Lawrence Livermore National Laboratory UCRL-52413.

[104] A. Calderon, "On an inverse boundary value problem," in *Seminar on Numerical Analysis and its Applications to Continuum Physics* (Brazilian Math. Society, Rio de Janeiro, 1980), pp. 65–73.

[105] J. Sylvester and G. Uhlmann, "A global uniqueness theorem for an inverse boundary value problem," *Annals of Mathematics* **125,** 153–169 (1987).

[106] A. Nachman, "Global uniqueness for a two-dimensional inverse boundary value problem," *Annals of Mathematics* **143,** 71–96 (1996).

[107] K. Astala and L. Päivärinta, "Calderón's inverse conductivity problem in the plane," *Annals of Mathematics-Second Series* **163,** 265–300 (2006).

[108] D. Barber and B. Brown, "Applied potential tomography," *Journal of Physics E: Scientific Instruments* **17,** 723 (1984).

[109] W. Daily, A. Ramirez, A. Binley, and D. LeBrecque, "Electrical resistance tomography," *The Leading Edge* **23,** 438 (2004).

[110] P. Holden, M. Wang, R. Mann, F. Dickin, and R. Edwards, "Imaging stirred-vessel macromixing using electrical resistance tomography," *AIChE Journal* **44,** 780–790 (1998).

[111] R. Williams, X. Jia, R. West, M. Wang, J. Cullivan, J. Bond, I. Faulks, T. Dyakowski, S. Wang, N. Climpson, J. Kostuch, and D. Payton, "Industrial monitoring of hydrocyclone operation using electrical resistance tomography," *Minerals Engineering* **12,** 1245–1252 (1999).

[112] D. Vlaev, M. Wanga, T. Dyakowski, R. Mann, and B. Grieve, "Detecting filter-cake pathologies in solid-liquid filtration: semi-tech scale demonstrations using electrical resistance tomography (ERT)," *Chemical Engineering Journal* **77,** 87–91 (2000).

[113] J. Kourunen, R. Käyhkö, J. Matula, J. Käyhkö, M. Vauhkonen, and L. Heikkinen, "Imaging of mixing of two miscible liquids using electrical impedance tomography and linear impedance sensor," *Flow Measurement and Instrumentation* **19,** 391–396 (2008).

[114] J. Kourunen, T. Savolainen, A. Lehikoinen, M. Vauhkonen, and L. Heikkinen, "Suitability of a PXI platform for an electrical impedance tomography system," *Measurement Science and Technology* **20,** 015503 (2009).

[115] W. Daily, A. Ramirez, D. LaBrecque, and J. Nitao, "Electrical resistivity tomography of vadose water movement," *Water Resources Research* **28,** 1429–1442 (1992).

[116] A. Friedman and M. Vogelius, "Determining cracks by boundary measurements," *Indiana Univ. Math. J* **38,** 527–556 (1989).

[117] G. Alessandrini and L. Rondi, "Stable determination of a crack in a planar inhomogeneous conductor," *SIAM Journal on Mathematical Analysis* **30,** 326–340 (1998).

[118] B. Brown, "Electrical impedance tomography (EIT): a review," *Journal of medical engineering & technology* **27,** 97–108 (2003).

[119] F. Santosa and M. Vogelius, "A backprojection algorithm for electrical impedance imaging," *SIAM Journal on Applied Mathematics* **50,** 216–243 (1990).

[120] K. Cheng, D. Isaacson, J. Newell, and D. Gisser, "Electrode models for electric current computed tomography," *IEEE Transactions on Biomedical Engineering* **36,** 918–924 (1989).

[121] E. Somersalo, M. Cheney, and D. Isaacson, "Existence and uniqueness for electrode models for electric current computed tomography," *SIAM Journal on Applied Mathematics* **52,** 1023–1040 (1992).

[122] A. Tihonov, "Solution of incorrectly formulated problems and the method of regularization," in *Soviet Math. Dokl*, Vol. 4 (1963), pp. 1035–1038.

[123] L. Heikkinen, M. Vauhkonen, T. Savolainen, and J. Kaipio, "Modelling of internal structures and electrodes in electrical process tomography," *Measurement Science and Technology* **12,** 1012 (2001).

[124] K. Karhunen, A. Seppänen, A. Lehikoinen, J. Kaipio, and P. Monteiro, "Locating reinforcing bars in concrete with Electrical Resistance Tomography," in *Concrete Repair, Rehabilitation and Retrofitting: 2nd International Conference on Concrete Repair, Rehabilitation and Retrofitting, ICCRRR-2, 24-26 November 2008, Cape Town, South Africa* (CRC, 2008), pp. 563–569.

[125] J. Webster, *Electrical impedance tomography* (Adam Hilger, 1990).

[126] K. Cheng, S. Simske, D. Isaacson, J. Newell, and D. Gisser, "Errors due to measuring voltage on current-carrying electrodes in electric current computed tomography," *Biomedical Engineering, IEEE Transactions on* **37,** 60–65 (1990).

[127] R. Cook, G. Saulnier, D. Gisser, J. Goble, J. Newell, and D. Isaacson, "ACT3: a high-speed, high-precision electrical impedance tomograph," *Biomedical Engineering, IEEE Transactions on* **41,** 713–722 (1994).

[128] T. Savolainen, J. Kaipio, P. Karjalainen, and M. Vauhkonen, "An electrical impedance tomography measurement system for experimental use," *Review of scientific instruments* **67,** 3605–3609 (1996).

[129] A. Wilkinson, E. Randall, J. Cilliers, D. Durrett, T. Naidoo, and T. Long, "A 1000-measurement frames/second ERT data capture system with real-time visualization," *Sensors Journal, IEEE* **5,** 300–307 (2005).

[130] L. Heikkinen, *Statistical estimation methods for electrical process tomography*, PhD thesis (University of Kuopio, 2005).

[131] D. Isaacson, "Distinguishability of conductivities by electric current computed tomography," *IEEE transactions on medical imaging* **5** (1986).

[132] M. Cheney and D. Isaacson, "Distinguishability in impedance imaging," *IEEE Transactions on Biomedical Engineering* **39,** 852–860 (1992).

[133] J. Kaipio, A. Seppänen, E. Somersalo, and H. Haario, "Posterior covariance related optimal current patterns in electrical impedance tomography," *Inverse Problems* **20,** 919 (2004).

[134] J. Kaipio, A. Seppänen, A. Voutilainen, and H. Haario, "Optimal current patterns in dynamical electrical impedance tomography imaging," *Inverse problems* **23,** 1201–1214 (2007).

[135] M. Vauhkonen, *Electrical impedance tomography and prior information*, PhD thesis (university of Kuopio, 1997).

[136] P. Vauhkonen, M. Vauhkonen, T. Savolainen, and J. Kaipio, "Three-dimensional electrical impedance tomography based on thecomplete electrode model," *IEEE Transactions on Biomedical Engineering* **46,** 1150–1160 (1999).

[137] P. Vauhkonen, *Image reconstruction in three-dimensional electrical impedance tomography*, PhD thesis (University of Kuopio, 2004).

[138] A. Papoulis, "Probability, random variables, and stochastic processes.," (1984).

[139] J. Melsa and D. Cohn, *Decision and estimation theory* (McGraw-Hill, 1978).

[140] V. Kolehmainen, *Novel approaches to image reconstruction in diffusion tomography*, PhD thesis (University of Kuopio, 2001).

[141] C. Lawson and R. Hanson, "Solving least squares problems," (1974).

[142] J. Nocedal and S. Wright, *Numerical optimization* (Springer verlag, 1999).

[143] T. Vilhunen, J. Kaipio, P. Vauhkonen, T. Savolainen, and M. Vauhkonen, "Simultaneous reconstruction of electrode contact impedances and internal electrical properties: I. Theory," *Measurement Science and Technology* **13,** 1848–1854 (2002).

[144] D. Phillips, "A technique for the numerical solution of certain integral equations of the first kind," *Journal of the ACM (JACM)* **9,** 84–97 (1962).

[145] J. Kaipio, V. Kolehmainen, M. Vauhkonen, and E. Somersalo, "Inverse problems with structural prior information," *Inverse problems* **15,** 713 (1999).

[146] D. Dobson and F. Santosa, "An image-enhancement technique for electrical impedance tomography," *Inverse problems* **10,** 317 (1994).

[147] M. Gehre, T. Kluth, A. Lipponen, B. Jin, A. Seppänen, J. Kaipio, and P. Maass, "Sparsity reconstruction in electrical impedance tomography: an experimental evaluation," *Journal of Computational and Applied Mathematics* (2011).

[148] M. Rantala, S. Vänska, S. Järvenpää, M. Kalke, M. Lassas, J. Moberg, and S. Siltanen, "Wavelet-based reconstruction for limited-angle X-ray tomography," *Medical Imaging, IEEE Transactions on* **25,** 210–217 (2006).

[149] P. Hua, J. Webster, and W. Tompkins, "A regularised electrical impedance tomography reconstruction algorithm," *Clinical Physics and Physiological Measurement* **9,** 137 (1988).

[150] P. Hua, E. Woo, J. Webster, and W. Tompkins, "Iterative reconstruction methods using regularization and optimal current patterns in electrical impedance tomography.," *IEEE transactions on medical imaging* **10,** 621 (1991).

[151] A. Adler and R. Guardo, "Electrical impedance tomography: regularized imaging and contrast detection.," *IEEE transactions on medical imaging* **15,** 170 (1996).

[152] P. Pinheiro, W. Loh, and F. Dickin, "Smoothness-constrained inversion for two-dimensional electrical resistance tomography," *Measurement Science and Technology* **8,** 293 (1997).

[153] M. Vauhkonen, D. Vadasz, P. Karjalainen, E. Somersalo, and J. Kaipio, "Tikhonov regularization and prior information in electrical impedance tomography," *IEEE transactions on medical imaging* **17,** 285–293 (1998).

[154] M. Vauhkonen, W. Lionheart, L. Heikkinen, P. Vauhkonen, and J. Kaipio, "A MATLAB package for the EIDORS project to reconstruct two-dimensional EIT images," *Physiological Measurement* **22,** 107 (2001).

[155] V. Kolehmainen, J. Kaipio, and H. Orlande, "Reconstruction of thermal conductivity and heat capacity using a tomographic approach," *International Journal of Heat and Mass Transfer* **50,** 5150–5160 (2007).

[156] G. Steiner and D. Watzenig, "Logarithmic parameter reconstruction in electrical tomography," *COMPEL: The International Journal for Computation and Mathematics in Electrical and Electronic Engineering* **28,** 879–891 (2009).

[157] K. Karhunen, A. Seppänen, A. Lehikoinen, and J. Kaipio, "Electrical Impedance Tomography for Imaging Concrete," in *10th International Conference on Biomedical Applications of Electrical Impedance Tomography (EIT 2009) combined with Workshop on Electromagnetic Inverse Problems, School of Mathematics, University of Manchester, UK* (2009).

[158] F. Santosa and M. Vogelius, "A computational algorithm to determine cracks from electrostatic boundary measurements," *International journal of engineering science* **29,** 917–937 (1991).

[159] V. Liepa, F. Santosa, and M. Vogelius, "Crack determination from boundary measurements—reconstruction using experimental data," *Journal of Nondestructive Evaluation* **12,** 163–174 (1993).

[160] K. Bryan and M. Vogelius, "Reconstruction of multiple cracks from experimental electrostatic boundary measurements," *Inverse Problems and Optimal Design in Industry* **7,** 147–167 (1993).

[161] F. Santosa, "A level-set approach for inverse problems involving obstacles," *ESAIM: Control, Optimisation and Calculus of Variations* **1,** 17–33 (1996).

[162] F. Hettlich and W. Rundell, "The determination of a discontinuity in a conductivity from a single boundary measurement," *Inverse Problems* **14,** 67–82 (1998).

[163] M. Brühl, M. Hanke, and M. Pidcock, "Crack detection using electrostatic measurements," *Mathematical Modelling and Numerical Analysis* **35,** 595–605 (2001).

[164] H. Kim and J. Seo, "Unique determination of a collection of a finite number of cracks from two boundary measurements," *SIAM Journal on Mathematical Analysis* **27,** 1336–1340 (1996).

[165] A. Elcrat and C. Hu, "Determination of surface and interior cracks from electrostatic measurements using Schwarz-Christoffel transformations," *International Journal of Engineering Science* **34,** 1165–1181 (1996).

[166] T. Bannour, A. Abda, and M. Jaoua, "A semi-explicit algorithm for the reconstruction of 3D planar cracks," *Inverse Problems* **13,** 899 (1997).

[167] S. Andrieux, A. Abda, and H. Bui, "Reciprocity principle and crack identification," *Inverse Problems* **15,** 59 (1999).

[168] A. Litman, D. Lesselier, and F. Santosa, "Reconstruction of a two-dimensional binary obstacle by controlled evolution of a level-set," *Inverse Problems* **14,** 685–706 (1998).

[169] C. Ramananjaona, M. Lambert, D. Lesselier, and J. Zolsio, "Shape reconstruction of buried obstacles by controlled evolution of a level set: from a min-max formulation to numerical experimentation," *Inverse Problems* **17,** 1087–1111 (2001).

[170] O. Dorn and D. Lesselier, "Level set methods for inverse scattering," *Inverse Problems* **22,** R67 (2006).

[171] D. Álvarez, O. Dorn, N. Irishina, and M. Moscoso, "Crack reconstruction using a level-set strategy," *Journal of Computational Physics* **228,** 5710–5721 (2009).

[172] K. Ito, K. Kunisch, and Z. Li, "Level-set function approach to an inverse interface problem," *Inverse problems* **17,** 1225–1242 (2001).

[173] K. Bryan and M. Vogelius, "A review of selected works on crack identification," *Geometric Methods in Inverse Problems and PDE Control* 25–46 (2004).

[174] V. Kolehmainen, S. Arridge, M. Vauhkonen, and J. Kaipio, "Simultaneous reconstruction of internal tissue region boundaries and coefficients in optical diffusion tomography," *Physics in Medicine and Biology* **45,** 3267–3284 (2000).

[175] O.-P. Tossavainen, V. Kolehmainen, and M. Vauhkonen, "Free-surface and admittivity estimation in electrical impedance tomography," *International Journal for Numerical Methods in Engineering* **66,** 1991–2013 (2006).

[176] D. Watzenig and C. Fox, "Posterior variability of inclusion shape based on tomographic measurement data," *Journal of Physics: Conference Series* **135,** 9 (2008).

[177] N. Hyvonen, H. Hakula, and S. Pursiainen, "Numerical implementation of the factorization method within the complete electrode model of electrical impedance tomography," *Inverse Problems and Imaging* **1,** 299–317 (2007).

[178] J. Chambers, P. Wilkinson, A. Weller, P. Meldrum, R. Ogilvy, and S. Caunt, "Mineshaft imaging using surface and crosshole 3D electrical resistivity tomography: A case history from the East Pennine Coalfield, UK," *Journal of applied geophysics* **62,** 324–337 (2007).

[179] F. Nguyen, S. Garambois, D. Chardon, D. Hermitte, O. Bellier, and D. Jongmans, "Subsurface electrical imaging of anisotropic formations affected by a slow active reverse fault, Provence, France," *Journal of applied geophysics* **62,** 338–353 (2007).

[180] E. Piegari, V. Cataudella, R. Di Maio, L. Milano, M. Nicodemi, and M. Soldovieri, "Electrical resistivity tomography and statistical analysis in landslide modelling: A conceptual approach," *Journal of Applied Geophysics* **68,** 151–158 (2009).

**Kimmo Karhunen**

# *Electrical Resistance Tomography Imaging of Concrete*

Concrete is the most used building material in the world. As the concrete infrastructure is increasingly deteriorating, the need for advanced testing methods for concrete is imminent. In this thesis, the feasibility of electrical resistance tomography (ERT) for non-destructive testing (NDT) of concrete is studied. The thesis considers, especially, localization of cracks and reinforcing bars inside concrete targets using ERT. The results show that ERT can characterize several electrical properties of concrete and has potential to become a practical tool for NDT of concrete.

UNIVERSITY OF
EASTERN FINLAND

Publications of the University of Eastern Finland
*Dissertations in Forestry and Natural Sciences*

ISBN 978-952-61-1232-9